

# AirCargoChallenge 2022

# Technical Report

Team #10

Aristotle Space & Aeronautics Team (ASAT)



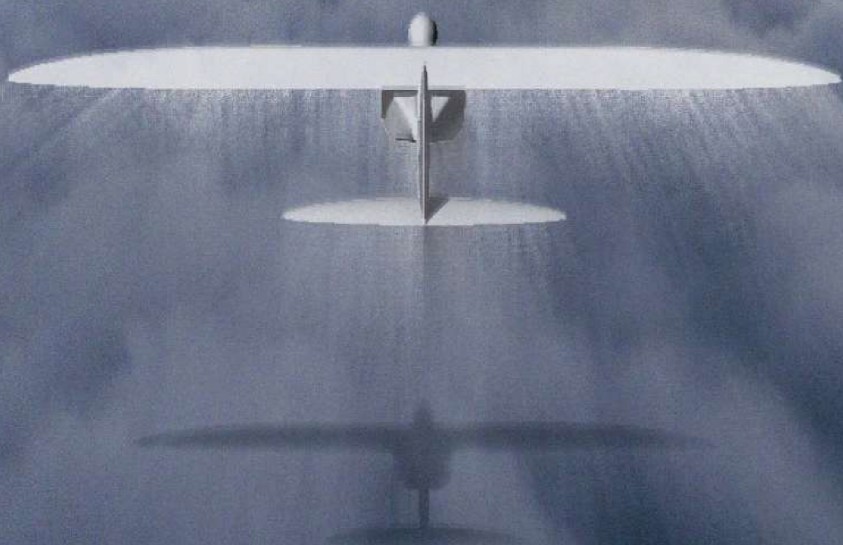


ARISTOTLE SPACE & AERONAUTICS TEAM

TECHNICAL REPORT

AIR CARGO CHALLENGE 2022

# AEOLUS



THESSALONIKI 2022

TEAM #10

## TABLE OF CONTENTS

<b>1</b>	<b>INTRODUCTION.....</b>	<b>2</b>
<b>2</b>	<b>PROJECT MANAGEMENT.....</b>	<b>2</b>
2.1	PROJECT STRUCTURE .....	2
2.2	COMMUNICATION.....	2
2.3	INFRASTRUCTURE.....	2
2.4	DOCUMENTATION.....	2
2.5	DESIGN & PROJECT PLANNING .....	3
2.6	TIMELINE .....	3
2.7	BUDGET .....	3
<b>3</b>	<b>MISSION ASSESSMENT &amp; DESIGN APPROACH .....</b>	<b>4</b>
<b>4</b>	<b>AERODYNAMICS DESIGN.....</b>	<b>5</b>
4.1	CONSTRAINT ANALYSIS.....	5
4.2	AIRFOIL SELECTION .....	5
4.3	WING & TAIL DESIGN .....	7
4.4	STABILITY & CONTROL .....	11
4.4.1	STABILITY DERIVATIVES.....	12
4.4.2	CONTROL SURFACES .....	13
4.5	PERFORMANCE .....	13
4.5.1	TAKE OFF DISTANCE .....	13
4.5.2	RATE OF CLIMB.....	14
4.5.3	POWER REQUIRED & POWER AVAILABLE ....	14
4.5.4	RANGE & ENDURANCE .....	14
4.5.5	LANDING DISTANCE .....	15
4.5.6	FLIGHT ENVELOPE .....	15
4.5.7	PROPULSION SYSTEM.....	15
4.5.8	PERFORMANCE SUMMARY .....	16
<b>5</b>	<b>STRUCTURAL DESIGN .....</b>	<b>16</b>
5.1	AIRCRAFT MASS & CG ESTIMATION .....	16
5.1.1	FIRST WEIGHT ESTIMATION .....	16
5.1.2	EMPTY WEIGHT ESTIMATION .....	17
5.1.3	CENTER OF GRAVITY .....	18
5.2	MATERIAL SELECTION & MANUFACTURING PROCESSES.....	18
5.2.1	MATERIAL SELECTION .....	19
5.2.2	MANUFACTURING PROCESSES.....	20
5.3	AIRCRAFT STRUCTURES .....	21
5.3.1	MAIN WING.....	21
5.3.2	FUSELAGE.....	24
5.3.3	EMPENNAGE .....	26
5.3.4	CARGO BAY .....	26
5.3.5	LANDING GEAR.....	27
5.3.6	CONTROL SURFACES .....	28
5.4	SUMMARY .....	28
<b>6</b>	<b>PAYOUT PREDICTION .....</b>	<b>29</b>
<b>7</b>	<b>AVIONICS .....</b>	<b>30</b>
7.1	UAV ELECTRICAL EQUIPMENT .....	30
7.2	FLIGHT DATA COLLECTION.....	30
<b>8</b>	<b>PROBLEMS ENCOUNTERED .....</b>	<b>30</b>
<b>9</b>	<b>OUTLOOK .....</b>	<b>30</b>
<b>10</b>	<b>ATTACHMENTS.....</b>	<b>31</b>
10.1	BUDGET & TIMELINE .....	32
10.2	NOMENCLATURE .....	34
10.3	CONCEPTUAL DESIGN PHASE.....	36
10.4	TECHNICAL DRAWINGS.....	37
<b>11</b>	<b>BIBLIOGRAPHY .....</b>	<b>38</b>

## 1 INTRODUCTION

Aristotle Space & Aeronautics Team ([ASAT](#)) is the largest aerospace student team in Greece, founded in 2015 by a group of Mechanical Engineering students with the passion of bringing theory into practice. Today, ASAT numbers more than 50 members. After our participation in ACC 2017 and 2019, we are determined to fly higher than we ever had before. Our expertise has grown through the years, and we are eager to gain new experiences through this competition, as well as hopefully climb up the rankings ladder. We also can't wait to meet new teams from all over the world.

## 2 PROJECT MANAGEMENT

### 2.1 PROJECT STRUCTURE

ASAT consists of three departments: Aeronautics, Rocketry and Marketing. Each department has a Project Leader, who is responsible for overseeing the work done. The departments consist of different subsystems, each of which has to do with a specific field of study. Every subsystem is supervised by a Coordinator and consists of multiple members. Given that ASAT and, in turn, Aeronautics, also conducts research on other aerospace-related topics, there are subsystems not directly involved with the ACC. Finally, the team is managed through a Board that oversees all operations, which consists of 4 members: the team's President, 2 Project Leaders and the Head of Marketing. Concerning the latter, and although not directly involved with the technical tasks of the team, the marketing department plays a huge role as well ensuring the funds from sponsorships that had to do both with the logistics and equipment needed for the competition. The Aeronautics department structure is depicted in Figure 2.1.1. The team operates under the auspices of the Faculty Advisor who is affiliated with the *Laboratory of Fluid Mechanics and Turbomachinery* ([LFMT](#)) of the *Aristotle University of Thessaloniki* ([AUTH](#)).

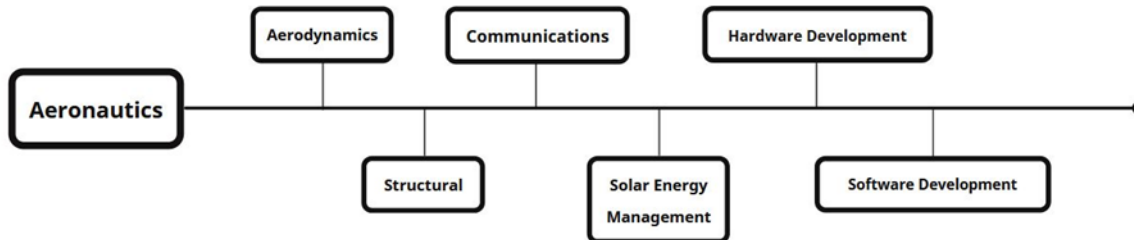


**Figure 2.1.1** Aeronautics project team structure.

### 2.2 COMMUNICATION

In our team, we value that good communication plays a huge role for correct and efficient management. In order to keep up with that, meetings are conducted once every week for each department, subsystem and local board. Other than meetings, we communicate daily through *Mattermost*, a communication platform with channels that are dedicated to specific topics regarding both management and project updates.

### 2.3 INFRASTRUCTURE

To keep our organization rigid, we hold our own infrastructure services. All of our digital infrastructure is self-hosted on our own servers. We use *Mattermost* as a communication platform, *OpenProject* for project tracking and task delegation, *4minitz* for minute keeping, and *NextCloud* as a cloud service. All of our members are registered on our *LDAP* database, while to maintain all these features we have our own IT department. Regarding our physical infrastructures, we have a laboratory inside the university campus where all technical and manufacturing tasks take place, as well as the meetings referenced above.

### 2.4 DOCUMENTATION

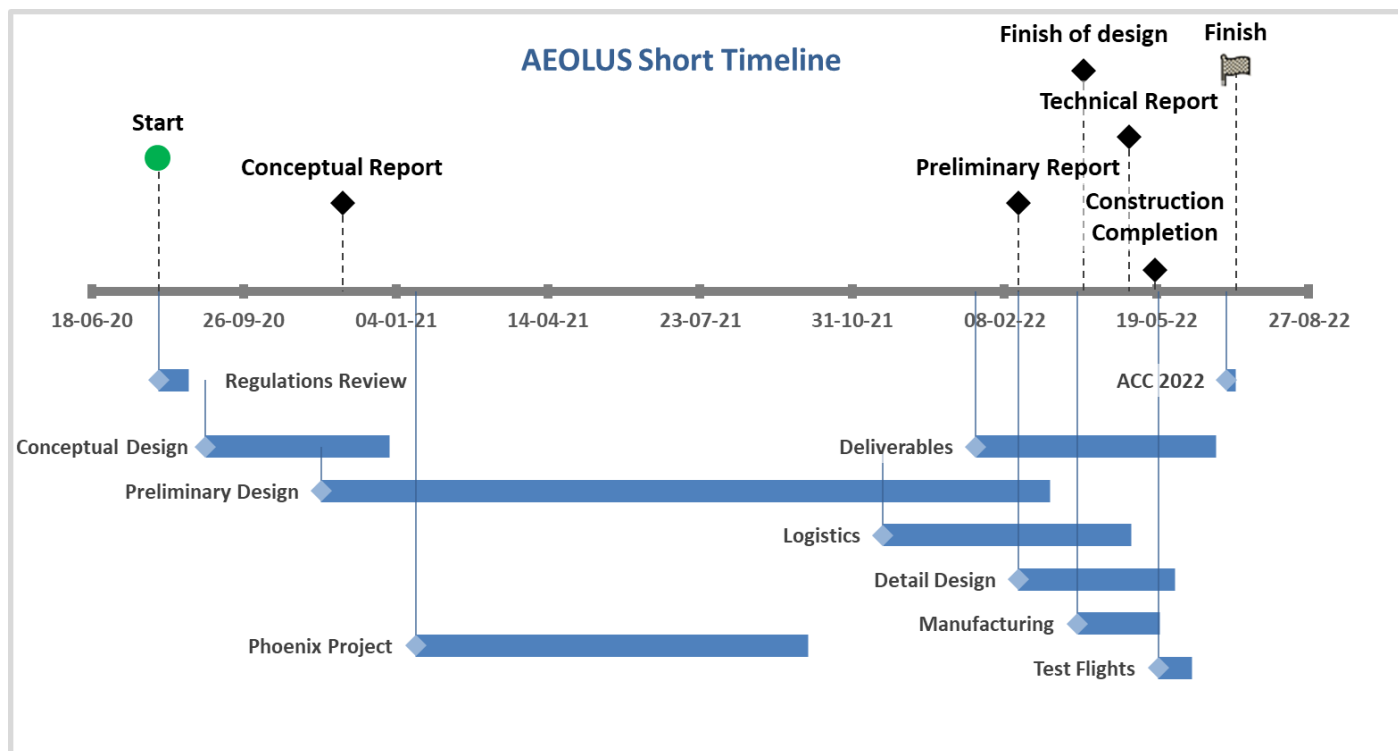
Having learnt the importance of keeping processes documented and passing our expertise to the next generations of ASAT members, we have developed a system of documentation, using a tree-like structure for the identification of report documents. Technical knowledge as well as organizational knowledge are well documented and stored for new members to read and learn from.

## 2.5 DESIGN & PROJECT PLANNING

The Aeronautics department follows the well-known phases of aircraft design: (1) Conceptual Design, which includes: Mission Assessment, first weight guess, initial sizing and in our case a Scoring Analysis too, (2) Preliminary Design, where all configurations (external and internal) are finalized, (3) Detail Design, which includes the construction of the UAV, integration, test flights and optimization. In terms of design operations, the Project Leader is responsible for organizing and keeping track of the technical work, utilizing the *OpenProject* platform. Moreover, in the weekly ACC sessions, progress is further discussed, and technical matters are further resolved between subsystems.

## 2.6 TIMELINE

A short timeline of the whole project can be found in the figure below. As it can be observed, the project AEOLUS began immediately after the announcement of the ACC 2021 regulations, although, a few months after the initiation of the preliminary phase the competition was delayed for 2022. In the extra year gained due to the delays we were occupied with the completion of the design and research for our new project: a solar UAV named PHOENIX. Furthermore, the quarantine time in Greece placed logistical barriers, due to order delays, lockdowns and not having access to our laboratory. An analytical timeline can be found in the *Attachment 10.1*.



## 2.7 BUDGET

Our team's budget mainly depends on sponsorships. A lot of sponsors directly provide us with materials and equipment. This is an estimated cost, not including the consumables expenses that will come up in the later stages of construction and assembly. As it can be observed, the expected cost for the project was €13,644, although the actual cost was approximately €10,174. The difference in values was covered directly from sponsorships, either in the form of machinery operations, or products. Regarding the largest amount of the actual cost also came from sponsorships, but in this case, it was deposited in our repository to use for the AEOLUS project. An analytical budget can be found in the attachment 10.1.

<b>AEOLUS SHORT BUDGET VARIANCE REPORT</b>				
		Budget	Actual	Variance + / -
<b>OVERVIEW</b>	<b>Total expenses</b>	€ 13,644.00	€ 10,174.75	€ (3,469.25)
<b>EXPENSE</b>		<b>Budget</b>	<b>Actual</b>	<b>Variance + / -</b>
<b>Manufacturing</b>	Manufacturing Budget Variance	€ 7,738.82	€ 1,924.60	€ (5,814.22)
	Percent of Expenses	56.7%	18,9%	37.8%
<b>Equipment</b>	Equipment Budget Variance	€ 1,097.80	€ 332.00	€ (765.80)
	Percent of Expenses	8.0%	3.3%	4.8%
<b>Logistics</b>	Logistics Budget Variance	€ 3,600.00	€ 6,150.00	€ 2,900.00
	Percent of Expenses	26.4%	60.4%	-34.1%
<b>Consumables</b>	Consumables Budget Variance	€ 362.81	€ 484.58	€ 121.77
	Percent of Expenses	2.7%	4.8%	-2.1%
<b>Electronics</b>	Electronics Budget Variance	€ 368.70	€ 540.20	€ 171.50
	Percent of Expenses	2.7%	5.3%	-2.6%
<b>Miscellaneous</b>	Miscellaneous Budget Variance	€ 475.87	€ 743.37	€ 267.50
	Percent of Expenses	3.5%	7.3%	-3.8%

### 3 MISSION ASSESSMENT & DESIGN APPROACH

Initializing with the mission assessment, the whole team gathered up to discuss about the aircraft's configuration. The main debate was between a pusher and a tractor configuration, where the pusher provided us with more endurance time while also reducing the total weight. However, after some careful consideration it was turned down due to the weight ultimately increasing by a small factor, a tractor's better propeller efficiency and less structural complexity and, finally, some stability considerations regarding the CG position (a pusher configuration is more likely to get tail heavy, which is undesirable). In addition, more design parameters were selected that had to do both with competition restrictions and our own design preferences. Namely, the UAV should not have been a rotary wing or a lighter-than-air aircraft, but an electric powered, fixed – wing aircraft able to carry as much payload as possible while also achieve as much range as possible. It should be noted that the type of payload is blood bags individually weighing 100 g or 300 g. On the other hand, aiming to a minimalistic aircraft, that is simple to manufacture, we chose a monoplane as the optimal aircraft configuration. The last step was a first total weight estimation with a major cooperation between the Aerodynamics Design and Structural subsystems. After that, some performance parameters were set from the competition which included the takeoff/landing distance being 60 m, the cruise altitude being 100 m and endurance being around 5 min.

Taking into consideration the mission and flight plan, some necessary factors that were either given, estimated, or demanded by the competition's regulations and varied with the propulsion system efficiency, were defined. An iterative process was followed between the constraint analysis described in *Section 4.1*, the mass estimation described in *Section 5.1.1* and material selection described in *Section 5.2.1*. The analysis consisted of typical values for the battery energy density and a cruise speed of 20 m/s that was selected after some trade studies. The result was a first weight estimation being 5.85 kg, where 3.3 kg was for payload, 2.2 kg was for the empty weight and the remaining was the battery mass.

## 4 AERODYNAMICS DESIGN

### 4.1 CONSTRAINT ANALYSIS

One of the first tasks in the aircraft's design process was to perform a constraint analysis via a constraint diagram. We based our analysis on literature<sup>[2]</sup> and developed a MATLAB tool in order to extract the  $W/S$  and  $P/W$  parameters. The necessary variables and their input values used in this iterative process are depicted in Table 4.1.1. All of the aerodynamic variables were either selected from statistical data or estimated. More specifically,  $C_{D,TO}$ ,  $C_{L,TO}$ ,  $C_{D,min}$  and  $k$  derived from literature<sup>[2]</sup> and the propeller efficiency ratios are discussed in Section 4.5.6. It must be noted that after the extraction of the constraint diagram,  $C_{L,TO}$  was calculated using the  $V_{LOF}$  and  $L = W$  when we noticed that the value was high enough. However, a change in the  $C_{L,TO}$  value would not affect or shift the design point. The correlations utilized to generate the constraint curves were taken from literature<sup>[2]</sup> and the result was the diagram seen in Figure 4.1.1.

UAV Requirements / Inputs			
Velocities	Flight altitude	Air density	Aerodynamic variables
$V_{cruise} = 20 \text{ m/s}$	$h_{sea} = 0 \text{ m}$	$\rho_{sea} = 1.225 \text{ kg/m}^3$	$C_{D,TO} = 0.036$ $n_{p,cruise} = 0.8$
$V_{max} = 25 \text{ m/s}$	$h_{cruise} = 100 \text{ m}$	$\rho_{cruise} = 1.2133 \text{ kg/m}^3$	$C_{L,TO} = 0.75$ $n_{p,TO} = 0.45$
$V_{stall} = 10 \text{ m/s}$	$h_{ceiling} = 120 \text{ m}$	$\rho_{ceiling} = 1.2133 \text{ kg/m}^3$	$C_{D,min} = 0.032$ $n_{p,climb} = 0.6$
$V_{LOF} = 1.2 \cdot V_{stall}$	Ground friction constant	Performance characteristics	$k = 0.049$
$V_{loiter} = 0.8 \cdot V_{cruise}$	$\mu = 0.04$	TO & landing distance = 60 m	
$ROC = 1.7 \text{ m/s}$			

Table 4.1.1. UAV requirements/ inputs.

The area which defines the design limits is the one above all the curves, satisfying the total need for power. Additionally, the values to the left of the vertical curves (that are independent of the wing loading - stall speed constraint) cover the corresponding constraint. This is because increasing the  $W/S$  past this limit will result in the wing having to withstand more load than it can handle and thus result in failure. Stalling speed and  $ROC$  were the constraints that extensively affected the wing loading. With that in mind, the design point was defined as the value combination that covered those two limitations. More specifically, it is the point  $[W/S, P/W] = [2.55 \text{ lb/ft}^2, 0.025 \text{ hp/lb}]$ .

At this point, it must be noted that since the airfoil selection process was performed alongside the constraint analysis, an iterative process was followed in order to predict the aircraft's  $C_{L,max}$  seen in Table 4.2.1. Keeping the power supplied by the propulsion system at  $260 \text{ W}$ , as referred in Section 4.5.6, we calculated the aircraft's weight with respect to the design parameter  $P/W$  which is  $W = 13.9 \text{ lb} = 6.3 \text{ kg}$ , a value very close to the first total weight estimation as seen in Section 5.1.1.

### 4.2 AIRFOIL SELECTION

Research for the selection of the wing's airfoil was based on the methodology and the recommendations analyzed in literature<sup>1,4</sup>. The followed procedures can be divided into three stages, first, in the theoretical estimation of the required lift coefficients, then in the analysis of various optional airfoils in a low fidelity tool (*XFLR5*) and finally in the selection of the most suitable airfoil, based on the tool's results and with guidance the criteria mentioned in the literature stated above. It should be noted that in order to choose the airfoil that best suits the mission, we took into consideration other requirements arising from mission assessment. In the case of AEOLUS, we focused on the following:

- sufficient thickness at the trailing edge area for the upcoming ailerons and flaps,
- quite aggressive shape, a highly cambered airfoil was desired in order to achieve a high lift coefficient,
- reasonably good stall behavior.

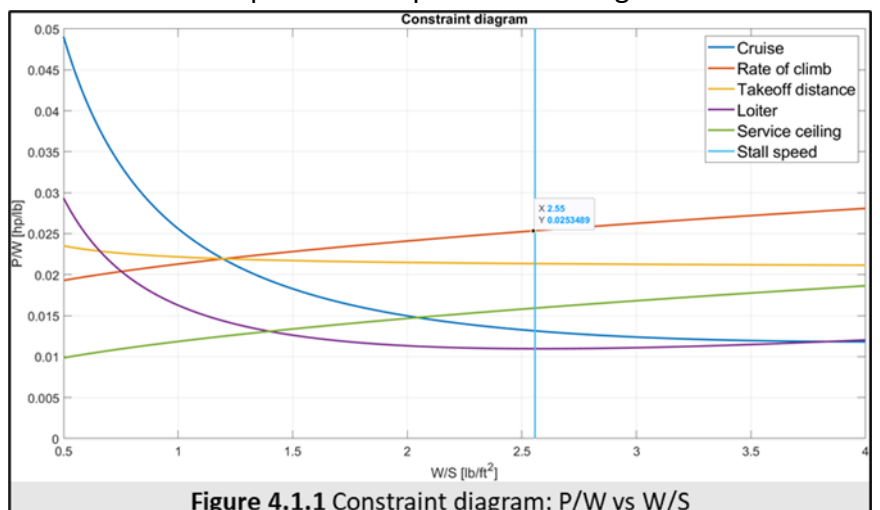


Figure 4.1.1 Constraint diagram:  $P/W$  vs  $W/S$

Considering all the above, we began the process of airfoil selection with a clear definition of flight requirements, while the following data were used for some initial numerical calculations. As mentioned above, based on bibliographical methodologies a series of calculations were made, including the aircraft's maximum lift coefficient, in order to arrive at an estimation for the airfoil maximum lift coefficient. The referenced numerical values were obtained as shown in Table 4.2.1.

The second stage of the airfoil selection process has to do with aerodynamic analyses using a low fidelity tool. The *XFLR5* software utilizes the *XFOIL* code and produces fast and accurate enough estimations for the lift & drag coefficients of the airfoil, based on the Panel Method. Note that in order to validate the results of this method, we cross – checked them with experimental data. Then, a first list of possible airfoils for the main wing was created and included high – lift airfoils. In order to meet the rest of the requirements set during mission assessment, we concluded in the *EPPLER* family. It is noted that the analysis was performed under the conditions dictated by the data:  $Re \approx 300000 - 400000$ , a range we expect to be in, and  $Ma \approx 0.059$ . Indicative results of the analysis using the *XFLR5* tool are listed in Figure 4.2.1 below, while the most important ones are presented summarized in Table 4.2.2.

The last step was to compare and evaluate the results from the low fidelity analysis. A measure of the airfoil's aerodynamic efficiency is the  $c_l/c_d$  ratio and the airfoil with the maximum value is *EPPLER 395*. The minimum  $c_{d,min}$  is for *EPPLER 392* while stall quality is quite similar for all the optional airfoils. However, the indicator we set as the most important, was to have the maximum  $c_{l,max}$ . This was in order not only to lift as much weight as possible, but also to bring off a lower  $V_{stall}$ , further away from the operation area. In the same time, the stall

Aircraft ideal cruise lift coefficient, $C_{L,c}$	0.508
Wing cruise lift coefficient, $C_{Lw,c}$	0.535
Airfoil ideal lift coefficient, $C_{l,i}$	0.594
Aircraft maximum lift coefficient, $C_{L,max}$	2.033
Wing maximum lift coefficient, $C_{L,w,max}$	2.14
Airfoil gross maximum lift coefficient, $C_{l,max,gross}$	2.378
Airfoil net maximum lift coefficient, $C_{l,max,net}$	2.378

Table 4.2.1. Aircraft performance parameters and coefficients estimation.

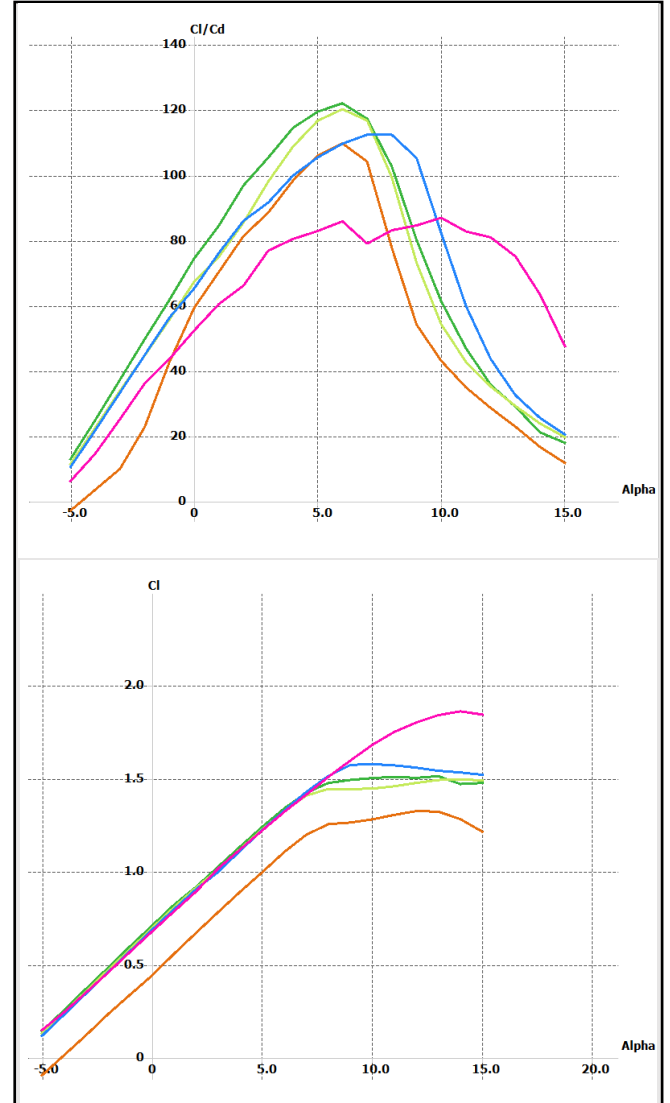


Figure 4.3.1 Airfoil analysis – XFLR5

Airfoil	$C_{l,max}$	$C_{d,min}$	$(C_l/C_d)_{max}$	$C_{l,\alpha=0}$	$\alpha$ for $C_{l,max}$
EPPLER 392 ●	1.33	0.0075	108.5	0.446	13°
EPPLER 395 ●	1.51	0.0096	120.4	0.710	13°
EPPLER 397 ●	1.49	0.01	118.6	0.697	14°
EPPLER 398 ●	1.58	0.01	111.4	0.688	10°
EPPLER 422 ●	1.86	0.013	85	0.679	14°

Table 4.2.2. Airfoil results – XFLR5.

angle was also increased. This guideline emerged from research on the scoring system done by our team's members. We concluded that lifting more payload is more beneficial (more points are given) than reaching a higher altitude within a shorter timeframe, while we aimed to a take-off distance reduction, even without using flaps. Taking all the above into consideration, we have chosen *EPPLER 422* for our aircraft's airfoil.

### 4.3 WING & TAIL DESIGN

Having extracted the constraint diagram and based on the first weight estimation, the Aerodynamic Design subsystem proceeded into the wing surface calculation. In more detail, for a  $6.36 \text{ kg}$  aircraft the wing area was calculated at  $S = 0.506 \text{ m}^2$ .

Taking into consideration that the assembled “flight ready” aircraft should fit into a rhombus-shaped box with an edge length ( $a$ ) of  $1.5 \text{ m}$  each, a detailed study on the competition’s size restrictions was carried out. The team’s aerodynamicists examined every possible angle between the edges and the rhombus diagonals combination. This procedure is described below. Changing the “A” angle of the rhombus, the diagonals,  $D_1$  and  $D_2$ , vary according to the trigonometrical equations:

$$D_1 = 2 \cdot a \cdot \sin\left(\frac{A}{2}\right) \quad | \quad D_2 = 2 \cdot a \cdot \cos\left(\frac{A}{2}\right)$$

It was not difficult to understand that the wingspan,  $b$ , extends along the diagonal  $D_1$  and receives values less than  $D_1$  length. In the same way, the fuselage length,  $L_f$ , extends along the diagonal  $D_2$  and receives values less than  $D_2$  length. In order to calculate the maximum wingspan and maximum fuselage length, we had to set some initial values as upper and lower limits. These values were for the wing’s tip chord and the horizontal tail span and selected per the experience gained from previous designs. Specifically, based on the weight estimation and thus the expected aircraft size, we set  $C_{tip,min} = 0.1 \text{ m}$  and  $b_{h,max} = 0.6 \text{ m}$ , limitations we would not surpass, meaning to have a smaller  $C_{tip}$  and a larger  $b_h$ . Then, the maximum wingspan results by subtracting the segment that remains “blank” due to the tip chords, named  $d_1$ , twice from the diagonal  $D_1$ , while similarly the maximum fuselage length was calculated and are both based on the equations below:

$$b_{max} = D_1 - 2 \cdot d_1 \quad | \quad L_{f,max} = D_2 - 2 \cdot d_2$$

After a first evaluation of the trade study’s results, the cases in which the fuselage length seemed disproportionate to the wingspan (“A” angle fluctuating between  $40^\circ - 75^\circ$  and  $105^\circ - 140^\circ$ ) were rejected. That is to say, that based on statistical data and experience with aircraft design the  $b/L_f$  ratio should not surpass the upper and lower values shown in Table 4.3.1. However, the final fuselage length was evolving as the design and internal component orientation were on progress taking several aerodynamic criteria into account. The correlation between these parameters is presented in Figure 4.3.1 and a summary of the results is presented in Table 4.3.1. It is more than obvious that the “rhombus restriction” was the main design guideline, imposing simultaneous procedures such as wing and tail sizing as well as stability analyses.

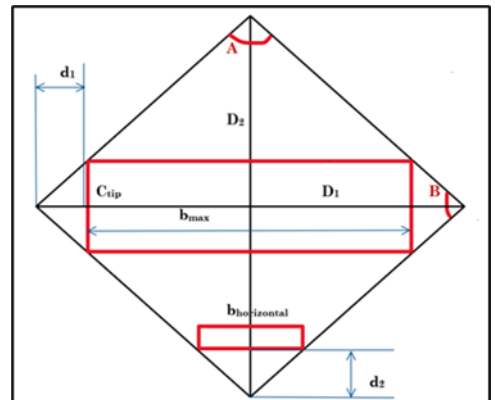


**Figure 4.3.1** Fitting of the aircraft configuration in the rhombus shaped box.

A [deg]	B [deg]	D <sub>1</sub> [m]	D <sub>2</sub> [m]	d <sub>1</sub> [m]	d <sub>2</sub> [m]	b <sub>max</sub> [m]	L <sub>f,max</sub> [m]	b/L <sub>f</sub>	AR aquired
80	100	1.928	2.298	0.060	0.252	1.809	1.795	1.008	6.47
85	95	2.027	2.212	0.055	0.275	1.918	1.662	1.154	7.27
87	93	2.065	2.176	0.053	0.285	1.960	1.607	1.220	7.59
90	90	2.121	2.121	0.050	0.300	2.021	1.521	1.329	8.07
93	87	2.176	2.065	0.047	0.316	2.081	1.433	1.453	8.56
95	85	2.212	2.027	0.046	0.327	2.120	1.372	1.545	8.88
100	80	2.298	1.928	0.042	0.358	2.214	1.213	1.825	9.69

**Table 4.3.1** Size restrictions based on the rhombus shaped box.

Therefore, to size the wing we had to choose an  $AR$  so the wing span to be determined. At this point, we recalled the results of the constraint analysis. Having a wing planform area of  $0.506 \text{ m}^2$  the corresponding  $AR$  was calculated for each of these seven cases considering the maximum wingspan. The  $AR$  values are shown in the 10<sup>th</sup> column of the Table 4.3.1. In the meantime, an additional procedure was performed in

order to study how the  $P/W$  parameter varies, according to the change of wing's aspect ratio. This sensitivity analysis was performed only for the cruise segment, as it is the one with the longest duration. The relevant diagram is presented in the Figure 4.3.2. Note that the inputs used to generate this diagram were the same with those used for the constraint analysis. As it can be observed, the  $P/W$  ratio decreases with an increasing  $AR$ . With that in mind, and having performed a number of stability analyses, we considered as a better option the case of a rhombus with both angles of  $90^\circ$ , that is a wing's  $AR$  close to 8. Consider that the weight increment due to a larger  $AR$  and the internal components configuration also contributed to that choice.

Moving on with the wing sizing, we had to make the wing's size and geometry more specific. We opted to make the wing semi - tapered (rectangular at a percentage of the wingspan). That was because a partly rectangular wing offers a bigger planform area and thus more lift than a straight - tapered one, while it produces a lift distribution close enough to the elliptical. Taking a step forward, we had to define the taper ratio and the percentage of the span at which the wing would be rectangular. According to literature<sup>[1]</sup>, for most unswept wings a taper ratio of about 0.4 alleviates the undesired drag effects of a totally constant - chord wing with the same  $AR$ . Bare in mind that a taper ratio closed to 0.4 could not be achieved without the rectangular part of the wing, as in that case an extremely large root chord length was derived. So, we performed analyses for a range close to  $\lambda = 0.4$ . With the same analyses the aerodynamics subsystem tried to conclude to the percentage value of the wing's rectangular part that leads to the optimum aerodynamic behavior. Indicatively, a comparison between the lift distribution on some of the potential configurations is presented in Figure 4.3.3, where the black colored curve represents the (ideal) lift distribution on an elliptical wing with the same span and surface.

The corresponding wing parameters are indicated in Table 4.3.2. As a result, the configuration which produced a lift distribution closer to the elliptical seemed to be Wing 4.

Moving on with the design, a number

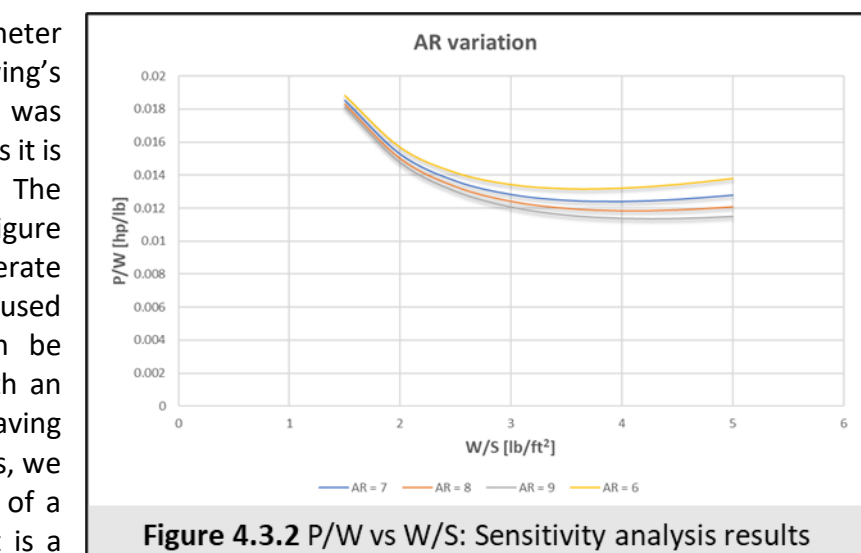


**Figure 4.3.2** P/W vs W/S: Sensitivity analysis results

Wings	Parameters				
	Span [m]	Rectangular Span [%]	Taper ratio ( $\lambda$ )	$C_{root}$ [m]	$C_{tip}$ [m]
Wing 1	2.08	60	0.35	0.286	0.1
Wing 2	2	50	0.4	0.3	0.12
Wing 3	2	82	0.45	0.267	0.12
Wing 4	2	56.5	0.41	0.29	0.12

**Table 4.3.2.** Wing parameters – XFLR5.

of wing parameters need to be assessed such as the wing placement, dihedral, twist and sweep angle. The wing was chosen to be a high wing as it better served our mission, which includes loading and unloading the cargo, while also preferred for better lateral stability, more "net" suction side as well as structural reasons.

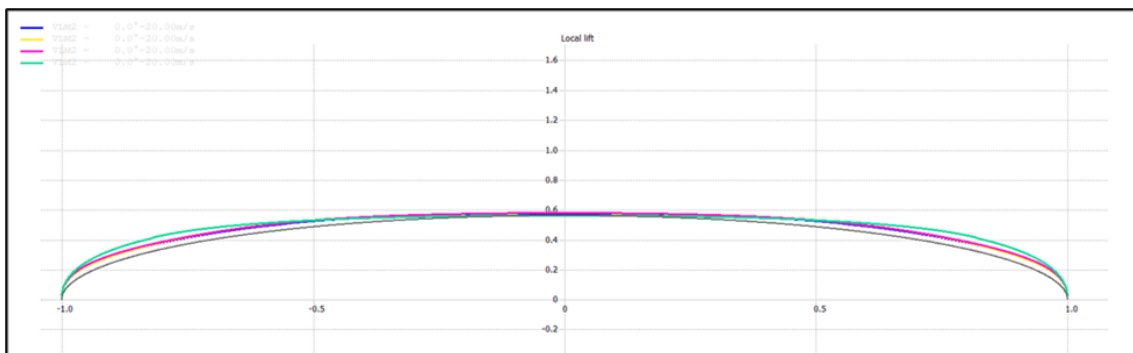


**Figure 4.3.3.** Lift distribution of 4 wing configurations compared to the elliptical one – XFLR5.

Having this in mind, applying a dihedral angle on the main wing was not practicable. Being satisfied with the aerodynamic characteristics of *EPPLER 422* and the performance of our UAV using this airfoil at the main wing, we decided to keep the same airfoil along the wingspan and not apply aerodynamic twist as well as geometric twist, since a change in the incidence angle along the span would be difficult to construct. Furthermore, we are flying at low speeds, so sweeping the wing would not only not improve the aircraft's behavior from an aerodynamic point of view but also deteriorate it reducing lift by the cosine of the sweep angle, and making the ailerons and flaps work poorly<sup>[1]</sup>.

Aiming to calibrate the center of gravity position (*CG*) and specifically to shift it forward, an evolutionary process was followed regarding the wing geometry. In more detail, keeping the dimensions constant, the wing configuration changed from a straight – leading edge to a front and back swept wing and finally to a straight trailing edge wing. The main configurations of this process are shown in Figure 4.3.4, while the third resulted to be the one with the optimal *CG* position, and thus we continued the design process with the specific wing configuration.

While defining the main wing, the tail design was also in progress as these two configurations are interdependent. During the conceptual design there were thoughts on conventional and V-tail configurations as well. The main advantage of the conventional geometry was that it provides sufficient stability & control at the lowest weight<sup>[1]</sup>. Other factors that contributed to select the conventional were that the required control system is less complex than that of the V-tail (ruddervator). The airfoils selected for the horizontal and vertical stabilizers are *NACA 0009* and *NACA 0012* respectively. Both of these

airfoils are symmetric since the design goal was not to produce more lift at zero angle of attack but to contribute to the overall aircraft stability. For the tail volume coefficients selection, we relied on values determined through statistical analyses that included various types of aircraft<sup>[1]</sup>. Using a MATLAB script<sup>[2]</sup>, a trade study was performed in order to result in the optimum tail arm ( $l_t$ ), based on a selected range of  $V_{HT}$ <sup>[1]</sup>, a constant  $V_{VT}$ <sup>[1]</sup> as well as the fuselage wetted area along the tail arm. The fuselage's frustum area extraction demanded a collaboration with the Structural subsystem, aiming to the estimation of the outermost diameters in that area. The output of this process is pointed on Figure 4.3.5. However, the size restrictions the rhombus shaped box set (Table 4.3.1), alongside with the fact that the tail arm of a tractor aircraft is about 60% of the fuselage's length<sup>[1]</sup> were considered. So, a tail arm close to 0.912 m was indicated. The remaining part of the fuselage, 0.608 m, was not only insufficient for the internal components configuration but also for the calibration for the aircraft's *CG*. After an iterative process, the selected  $l_t$  came out to be 0.85m leading us to the tail planform areas calculation. It should be noted that due to the conventional configuration, both horizontal and vertical tails'  $l_t$  approximate the same value.

Moving on with the tail sizing, several other parameters had to be defined such as the tail *AR*. For the horizontal tail it was initially calculated at 5.8, a value outside of the suggested range, [6, 10]<sup>[1]</sup>. Therefore, the  $b_h$  decreased to 0.55 m altering the  $AR_h$  to 4.8 without affecting the wing size. As for the vertical stabilizer, there were no critical size restrictions implemented by the regulations, so the  $AR_v$  was selected based on statistical data, having as a criterion the

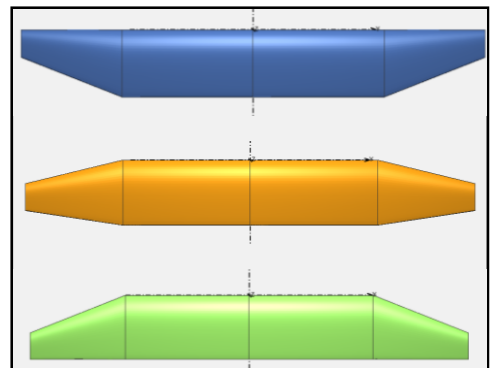


**Figure 4.3.4** Evolution of wings' configuration during conceptual design

Aircraft category	$V_{HT}$	$V_{VT}$
Homebuilt	0.50	0.04
General aviation - single engine	0.70	0.04
General aviation - twin engine	0.80	0.07

**Table 4.3.3.** Typical values for tail volume coefficients.

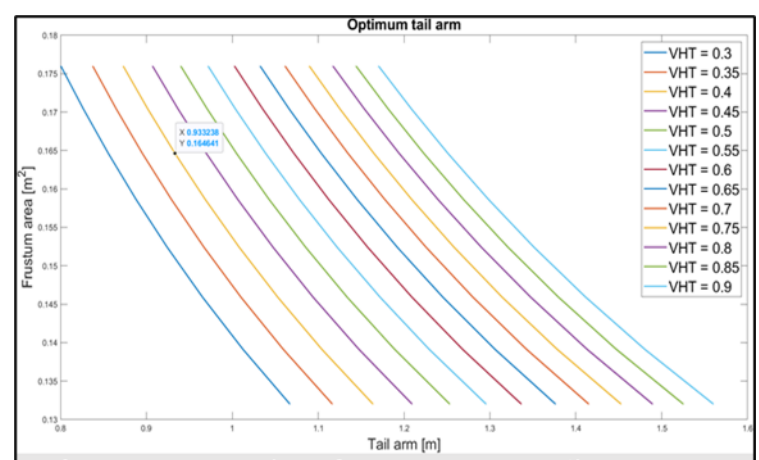


**Figure 4.3.5** Fuselage frustum area vs tail arm – VHT variation.

aerodynamic efficiency acquiring. Concerning the taper ratios, we opted for values within the suggested range, [0.3, 0.6]<sup>[1]</sup>.

	Surface area [ $m^2$ ]	Span [m]	Aspect ratio	Taper ratio	Root chord [m]	Tip chord [m]
Wing	0.506	2	7.9	0.41	0.29	0.12
Horizontal tail	0.0632	0.55	4.78	0.53	0.15	0.08
Vertical tail	0.0375	0.3	2.4	0.67	0.15	0.01

Table 4.3.4. Final geometric dimensions of wing and tail (conceptual design).

The overall configuration of AEOLUS was validated with a parametric tool developed by the team which is based on a literature manual<sup>[3]</sup>. The aerodynamic performance results are summarized in Figure 4.3.6.

Going through the last stages of design, the change of the wing's geometry to elliptical was considered as an appropriate optimization in order to achieve a lift distribution and an aerodynamic behavior closer to the ideal one. Despite the conversion to elliptical geometry, there would be still a rectangular section in the middle of the wing. Therefore, we can speak of a wing with elliptical tips, which was geometrically achieved by intersecting left and right two identical ellipses.

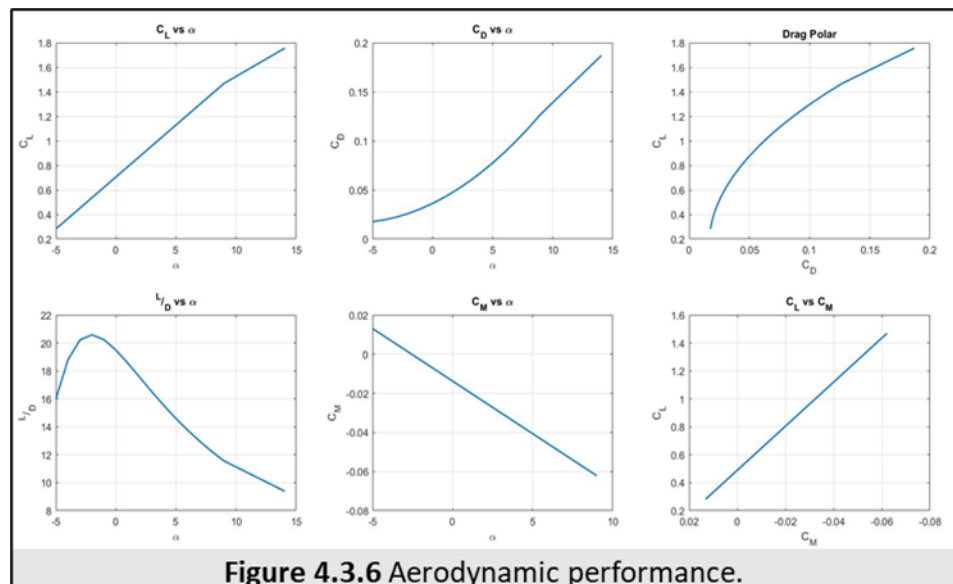


Figure 4.3.6 Aerodynamic performance.

This optimization was achieved with the development of a MATLAB script that takes as inputs the wing's planform area, span and root chord length returning the partly elliptical geometry. An additional necessary input was the point where the 2 elliptical lines would join (given as a percentage of the root chord length). The options, regarding this input, were between  $1/4$ ,  $2/4$ ,  $3/4$  and the "custom" as seen in Figure 4.3.7.

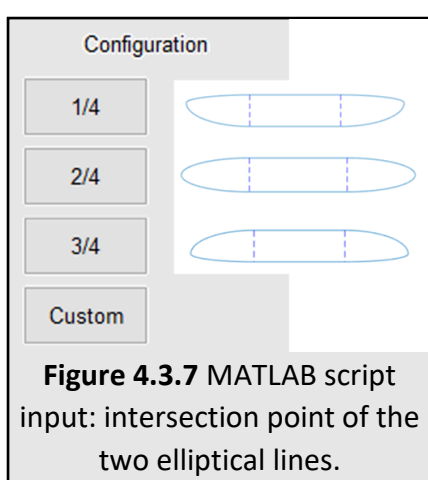


Figure 4.3.7 MATLAB script input: intersection point of the two elliptical lines.

After a variety of geometries tested and lots of iterations, we concluded in the configuration shown in Figure 4.3.8. Specifically, the two ellipses intersect at the 75% of the wing's root chord (ellipses combine at 0.2175 m along the x-axis) creating the final wing configuration, which is a 2m span wing, with an area of  $0.506 m^2$ , a root chord length of 0.29 m and a rectangular sector in the middle with length 0.8358 m. The two ellipses were chosen to intersect at  $3/4$  of the wing's root chord so as to be closer to the previous configuration – a straight trailing edge wing but structural as well as aesthetic criterions were also considered. It is more than obvious that the wing's dimensions, determined in the conceptual design phase, stayed unvaried during the conversion to elliptical geometry. The only change that was implemented had to do with the middle rectangular section, which decreased to 41.79% of the semispan

in order to keep the wing's planform area constant.

The same optimization procedure was followed both for the horizontal and vertical stabilizers' configurations. The difference compared to the wing and the vertical stabilizer is noticed in the fact that the horizontal stabilizer does not include a rectangular part but is fully elliptical. It must be noted that in order to keep the horizontal stabilizer's area constant and to stay as close as possible to the late conceptual tapered configuration, the span decreased to 0.536 m.

Confirmation of such elliptical geometries as well as checking their aerodynamic behavior and stability were not possible through the available low fidelity tools such as XFLR5 or our MATLAB scripts. However, the results of these analyses were not expected to be extremely different from those of the last stage of the conceptual design (see Table 4.3.4 and Figure 4.3.6). That was because the surfaces and the majority of the basic dimensions stayed unvaried, so the stability (e.g. trim diagram) characteristics would only change slightly, while the performance is expected to improve.

#### 4.4 STABILITY & CONTROL

The static stability consists of the ability of the aircraft to return to its equilibrium point after experiencing a disturbance. That is when e.g. a gust of wind results in a pitch up movement, the aircraft must have the ability to create a pitch down moment to return back to its initial position without any input from the pilot (this applies to disturbances in every direction). After a statically stable design is created, we also checked the slope of the " $C_M$  vs  $\alpha$ " curve in order to ascertain that the pitching moment coefficient slope aligned with the corresponding literature guidelines for optimal pitching stability. Moreover, the aircraft must also be dynamically stable. After a disturbance is applied the aircraft will oscillate for some time around the neutral position. The dynamic stability will show the rate of decay of those oscillations. We, of course, want the oscillations to disappear after some time but again the rate of decay is important in order to obtain the best behavior. This section is referred to the stability of the final configuration of the aircraft. The semi-tapered equivalent wing was used as a basis for our analysis and thus the wing contribution<sup>[11]</sup> is:

$$C_{M_{cg,w}} = C_{M_{ac,w}} + (C_{L_{0,w}} + C_{L_{\alpha,w}} * \alpha_w) * \left( \frac{\bar{x}_{cg}}{c} - \frac{\bar{x}_{ac}}{c} \right) \quad (2.6, \text{Ref. 11})$$

Estimating the fuselage contribution was based on a discrete model of its geometry, where we split the fuselage into 13 finite sections<sup>[3]</sup> ( $\Delta x, w_f$ ) along its length and tried to create a mean geometrical shape of each section that approximated the real geometry. Moreover, we included the cargo bay's shape and considered it part of the fuselage for this analysis.

$\Delta x$	0.0948	0.0697	0.0697	0.1533	0.0700	0.2100	0.0763	0.1608	0.0990	0.0990	0.0990	0.0990
$w_f$	0.045	0.076	0.078	0.067	0.174	0.171	0.118	0.070	0.286	0.286	0.286	0.286

Table 4.4.1. Fuselage length ( $\Delta x$ ) and fuselage width ( $w_f$ ) for each increment.

The fuselage contribution<sup>[11]</sup> is:

$$C_{M_{cg,f}} = \frac{k_2 - k_1}{36,5 * S * c} * \sum_{x=0}^{x=1} [w_f^2 * (\alpha_{0,w} + i_f) * \Delta x] + \frac{1}{36,5 * S * c} * \sum_{x=0}^{x=1} [w_f^2 * \frac{\partial \varepsilon_u}{\partial \alpha} * \Delta x] * \alpha_w \quad (2.30, 2.32, \text{Ref. 11})$$

Generally, the contributions of the wing and fuselage make for an unstable aircraft which means that the  $C_M$  slope is positive. This is the reason why we included a tail in the aircraft's design where the most crucial, among others, is to make the aircraft statically stable. The horizontal tail contribution<sup>[11]</sup> is:

$$C_{M_{cg,h}} = \eta * V_{HT} * C_{L_{a,h}} * (\varepsilon_0 + i_w - i_h) - \eta * V_{HT} * C_{L_{a,h}} * (1 - \frac{d\varepsilon}{d\alpha}) * \alpha \quad (2.24, \text{Ref. 11})$$

In order to calculate the contributions of each segment of the aircraft some parameters needed to be assessed and are listed in Table 4.4.2 below.

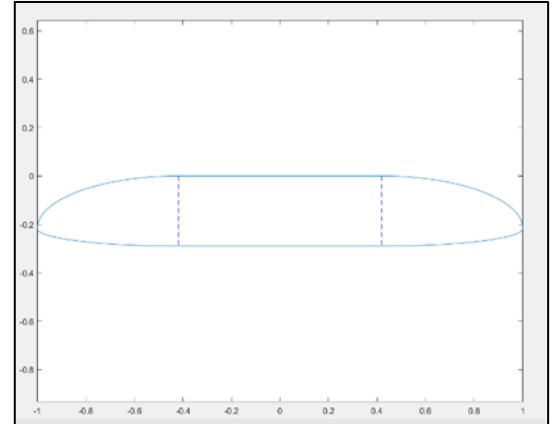


Figure 4.3.8. Final wing configuration.

$C_{m,ac,w}$	$C_{L,0,w}$	$C_{L,\alpha,w}$	$x_{cg}$	$x_{ac}$	$k_2 - k_1$	$\alpha_{0,w}$	$i_w$	$i_h$	$i_f$	$\eta$	$C_{L,a,h}$	$\epsilon_0$	$de/da$
0.0305	0.5307	0.08	36.5%	42.8%	0.9635	-6.6	2°	-2°	0°	0.9	0.0679	2.45	0.0066

Table 4.4.2 Crucial stability parameters.

These aerodynamic coefficients and  $x_{ac}$  are all calculated using the in house tool<sup>[2]</sup>, also mentioned in Section 4.3, while  $x_{cg}$  was selected with the collaboration of the aerodynamics design and structural subsystems accordingly so that the aimed static margin is 6.35%, which is nominal for the aircraft's behavior, could also be achieved during construction. In addition, the incidence angles of the wing and horizontal tail were set to 2° and -2° respectively mainly for the takeoff segment as it will be mentioned in Section 4.5.1 while also achieving an almost nominal stability which allowed us to not largely trim during cruise as the weight and  $CG$  remain constant. The overall behavior of the aircraft's  $C_M$  around the  $CG$  ( $C_M$  vs  $\alpha$ ) can be seen in Figure 4.3.6. The aircraft takeoff weight equals to the weight during landing. Moreover, the payload will not change position during flight, thus the  $CG$  will remain constant. This means that there will be only one position where  $C_M$  will remain equal to zero and no moment will be created. During the design phase it was easy to consider a proper configuration at which the  $C_M$  would remain zero during cruise. This can be presented with a " $C_L$  vs  $\alpha$ " and a " $C_M$  vs  $C_L$ " diagram around the  $CG$  as seen in Figure 4.4.1. The most aft and most forward positions of the  $CG$  occur when we change the position and weight of the payload accordingly in order to achieve the most extreme values for the  $CG$ . These positions of the  $CG$  cannot be exceeded and thus set the base for the most extreme stability margins. The most aft position of the  $CG$  is at 69% of the wing's  $MAC$  and the most forward at 23% of the wing's  $MAC$ , from the wing's leading edge. We can observe that the most aft position is way past the aircraft's aerodynamic center. This means that in no circumstance shall we approach this limit as a  $CG$  aft of 42.8% of the wing's  $MAC$  will make the aircraft unstable. A complete trim diagram shall also include the most aft and most forwards positions of the  $CG$ . These curves can be directly calculated with regard to the reference curve following the Procedure 1<sup>[3]</sup>.

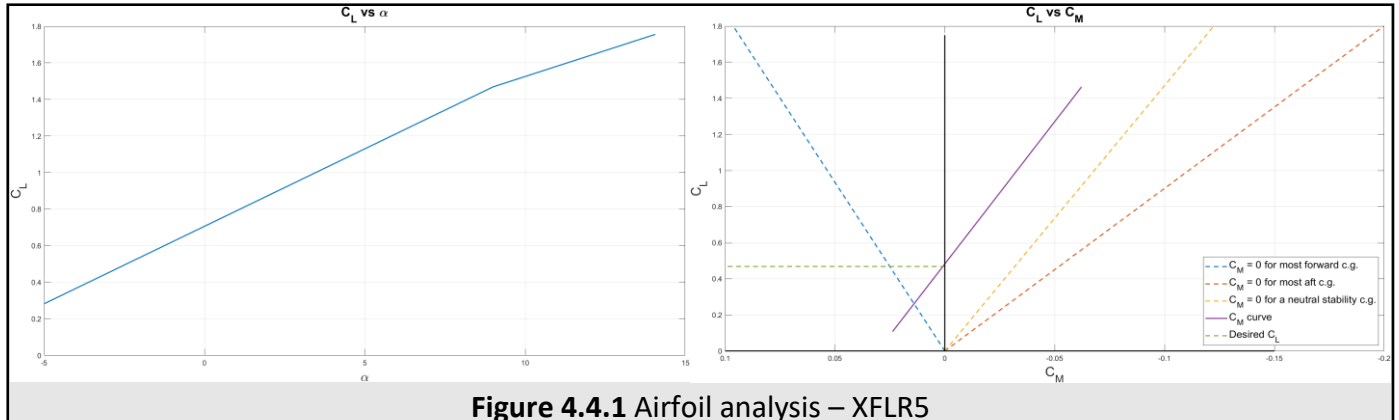


Figure 4.4.1 Airfoil analysis – XFLR5

#### 4.4.1 STABILITY DERIVATIVES

The stability derivatives indicate the static and dynamic stability behavior of the aircraft. They show the rate of change of pitching, yawing and rolling moments with respect to the angle of attack, the sideslip angle and the roll angle for the static stability and with respect to pitch, yaw and roll rate for the dynamic stability. We were mostly focused on calculating the longitudinal stability derivatives, since they serve the trim diagram as mentioned above. Nevertheless, all of them are important for a stable design. Some typical ranges for the derivatives are suggested in literature<sup>[4]</sup>, and they served as a comparison platform for our calculations<sup>[4]</sup> during the cruise segment and shown in Table 4.4.1.1.

Derivatives	$C_{m,\alpha}$	$C_{m,q}$	$C_{n,\beta}$	$C_{n,r}$	$C_{n,p}$	$C_{l,p}$	$C_{l,r}$
Calculated values [deg <sup>-1</sup> ]	-0.00537	-0.17070	0.00116	-0.00185	0.00059	-0.00793	0.00236
Proposed range [deg <sup>-1</sup> ]	[-0.026, -0.0052]	[-0.698, -0.087]	[0.00087, 0.00698]	[-0.017, -0.0017]	-	-	-

Table 4.4.1.1. Stability derivatives: calculated and suggested values.

#### 4.4.2 CONTROL SURFACES

In this section, the design process of the control surfaces is presented as well as the calculation of the elevator, rudder and aileron effectiveness which are shown through the control derivatives. The flaps design was based on the takeoff performance studies in order to achieve a  $40\text{ m}$  takeoff while the rest of the control surfaces' sizing was based on the type of the aircraft and consisted of a connection between the chosen span and chord of the control surface. We concluded that the flaps would span from  $0.082\text{ m}$  of the semi-span up to  $0.6\text{ m}$  and will have a constant cord of  $0.0513\text{ m}$  which accounts for 17.7% of the wing's chord. This results in a total area of  $0.053\text{ m}^2$  which is 10.5% of the wing's area.

Taking the flaps' design into consideration, the ailerons should deviate by a certain distance from the flaps, so as to reinforce the wing with ribs, and could extend up to the end of the wing's span. A rough estimation, where the ailerons start from 60% of the semi span and extend to the wingtip led to an aileron span of 40% of the wing's span. Keeping that in mind and based on Figure 6.3<sup>[3]</sup> the aileron chord should be between 20% - 25% of the wing's chord. After some careful consideration on what suited best to our design and construction, the aileron span dimensioned from  $0.636\text{ m}$  to  $0.97\text{ m}$  of the wing's semi-span having an almost constant chord (due to the elliptical geometry) of  $0.0675\text{ m}$ . This gave us a surface of  $0.045\text{ m}^2$  and in turn the ratio  $S_a/S$  was calculated at 8.8%, a value within the suggested margin of 5% - 10%.

Moving on with the elevator and rudder, based on Table 6.5<sup>[3]</sup> our UAV could be classified in the category of *GA-single engine*, so a first estimation for the elevator was around 45% of the horizontal tail chord, while for the rudder was around 40% of the vertical tail chord. We opted to take advantage of the whole span for both control surfaces, with a mild cut on the rudder's surface where it meets the elevator so as to enable the latter to move freely to the upward direction. The chord remained constant along the span consisting the  $0.033\text{ m}$  (45%) for the elevator and  $0.0468\text{ m}$  (40%) for the rudder, in such manner that  $0.018\text{ m}^2$  and  $0.01404\text{ m}^2$  could be exploited. In the same way, the ratios  $S_e/S_h$  and  $S_r/S_v$  were calculated at 28.5% and 37.4%, while their suggested values should vary between 15% - 40% and 15% - 35% respectively. The final step was to calculate the corresponding effectiveness of all the control surfaces and examine if they meet our demands.

Derivatives	$C_{L,\delta e}$	$C_{m,\delta e}$	$C_{n,\delta r}$	$C_{l,\delta a}$
Calculated values [deg <sup>-1</sup> ]	0.0038	-0.012	-0.00091	0.0037

Table 4.4.2.1 Control derivatives: calculated values.

#### 4.5 PERFORMANCE

The performance analysis was conducted throughout every design phase of the aircraft. However, the changing factor was the amount of validated data and consequently the results' level of detail. During the conceptual design phase simplified equations were used that required very few parameters to be known, some of which needed to be assumed. The parameters known were generally calculated using the constraint diagrams, the weight estimation and the initial sizing of the wing. The parameters that needed to be assumed were mostly statistical values deriving from thousands of previous aircraft designs. During the preliminary design phase, more data about the aircraft were validated. From that point on, the equations get more detailed, the results more precise and optimization was performed. Lastly, in the detailed design phase optimization proceeded and flight tests will be performed in order to evaluate the results, validate the tools and calibrate them if necessary. In this section, the UAV's performance parameters are quoted in detail. Note that the performance parameters are calculated for the maximum takeoff weight of  $5.86\text{ kg}$  as mentioned in Section 5.1.2.

##### 4.5.1 TAKE OFF DISTANCE

During the scoring analysis our team opted to pursue the  $40\text{ m}$  ground roll and in order to achieve this goal a weight reduction as well as the addition of flaps were needed. As said above, in the conceptual design a simplified equation was used based on  $W/S$ ,  $T/W$  and  $C_{L,max}$ . Both  $W/S$  and  $T/W$  were known values, but  $C_{L,max}$  was obtained with low accuracy using airfoil data and estimations. However, the inaccuracy of the value calculated during that phase was noticeable and thus further investigation was needed. Trade studies and optimization took place including control surfaces sizing. We were able to study different sizes of flaps and deflections to test our limits. Based on the literature manual<sup>[3]</sup> we can achieve  $\Delta C_L$  equal to 0.63 for a

30° flap deflection as shown in Figure 4.5.1.1. The required  $C_L$  during liftoff is 1.28 for  $V_{LO} = 12 \text{ m/s}$ , which is 1.2 times greater than the  $V_{stall}$  and within the range set by the literature. Expecting the liftoff to happen with minimal rotation at an angle of attack close to 0° based on our landing gear configuration, as mentioned in Section 5.3.5, means we achieve a larger than necessary  $C_L$ . However, low-fidelity tools cannot perfectly simulate the aircraft's geometry and thus the achieved value should deviate. But the flap deflection is within the suggested range and thus during test flights we can calibrate the configuration to achieve the best results. For the takeoff distance, although in the late stages of the preliminary design the obtained value was 36.6 m, the ultimate results would come from the test flights.

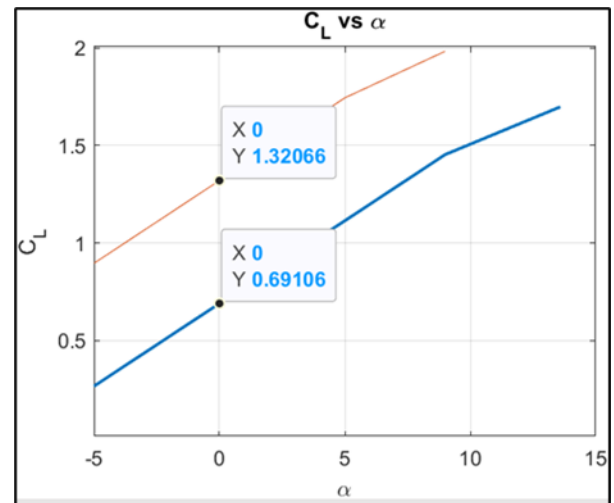


Figure 4.5.1.1  $C_L$  vs  $\alpha$  with 30° flaps.

#### 4.5.2 RATE OF CLIMB

The most important parameter during climb is the aircraft's maximum rate of climb ( $ROC$ ) which will eventually give the shortest time to reach a certain altitude. During the preliminary design we used the same equations as in the conceptual phase but more information about the aircraft was available and more parameters were calculated instead of assumed. The result is 3.3 m/s with an angle of 7.9° and velocity of 24 m/s. In the meantime, using a diagram similar to Figure 3.6.3.1, where the propeller efficiency varies during climb, we calculated the excess power that corresponds to the maximum difference between the power available and power required at a given velocity. The maximum excess power calculated is 162.8 W and the maximum  $ROC$  is 2.8 m/s. Also, note that this value corresponded to the sea level climb properties but due to minimal change in density from 0 – 100m was close to the mean value of the  $ROC$  during the mission. These values will be checked through the scheduled test flights in order to validate them and calibrate our tools.

#### 4.5.3 POWER REQUIRED & POWER AVAILABLE

A graph containing the power required/available can be sketched to interactively indicate the boundaries set by the engine during cruise. The required thrust equals to the drag produced during cruise for different velocities and its values can be calculated from  $C_D$  using the aircraft's drag polar. For a propeller driven airplane the available thrust varies with velocity. The thrust produced by the propeller reaches its maximum value at zero velocity (static thrust) and decreases constantly with increasing velocity until it reaches zero at sonic speeds. On the contrary, the power available remains constant as the power produced by the electric motor is constant. The corresponding graph is shown in Figure 4.5.3.1. and confirms that the required power is satisfied for the cruise velocity chosen during the mission assessment. Based on the mission, the altitude change is such that the change in density is minimal. This means that for the mission purposes the rate of climb will not change dramatically and thus the service and absolute ceilings will not affect our design because their values significantly exceed the flight area.

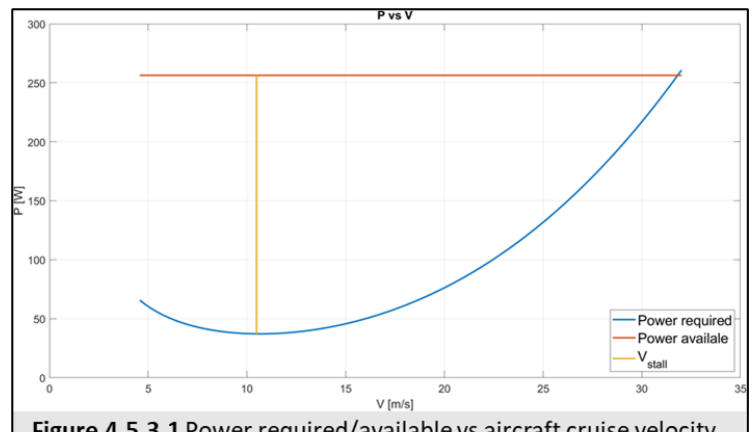


Figure 4.5.3.1 Power required/available vs aircraft cruise velocity.

#### 4.5.4 RANGE & ENDURANCE

The range of the aircraft is worth mentioning only during the flight segment where it contributes to the points scored, being the cruise segment. During that time the aircraft will fly at a constant velocity of 20 m/s for as much as 120 s per the competition. Thus, the total achievable range comes up to 2400 m. For the endurance, with a cooperation between the aerodynamics design and avionics subsystems we managed to

estimate its value to be 9 min. which covered up the competition's requirements and also added a safety factor so as we don't lose control of the engine during flight.

#### 4.5.5 LANDING DISTANCE

In the course of the conceptual design phase, similarly to *Section 4.5.1*, we used simple equations and assumptions based on wing loading, produced lift and  $C_{L,max}$ . Advancing into the preliminary design more details were available and through trade studies and optimization we gather more data but the same equations. The calculated landing distance is 52.6 m, with a 40° flap deflection, a result that is within the runway limits. The ultimate step would be to validate them through the scheduled test flights.

#### 4.5.6 FLIGHT ENVELOPE

The performance analysis is summarized in the flight envelope, a typical  $V - n$  diagram that depicts the region where the aircraft can fly without stalling, breaking apart or reaching its maximum velocity. For the structural integrity of the aircraft a positive and a negative limit load factor of 1.5 were chosen describing the limit above which the aircraft will continue its mission receiving minimal damage. From these values the ultimate positive and negative load factors were calculated, which are 1.5 times greater

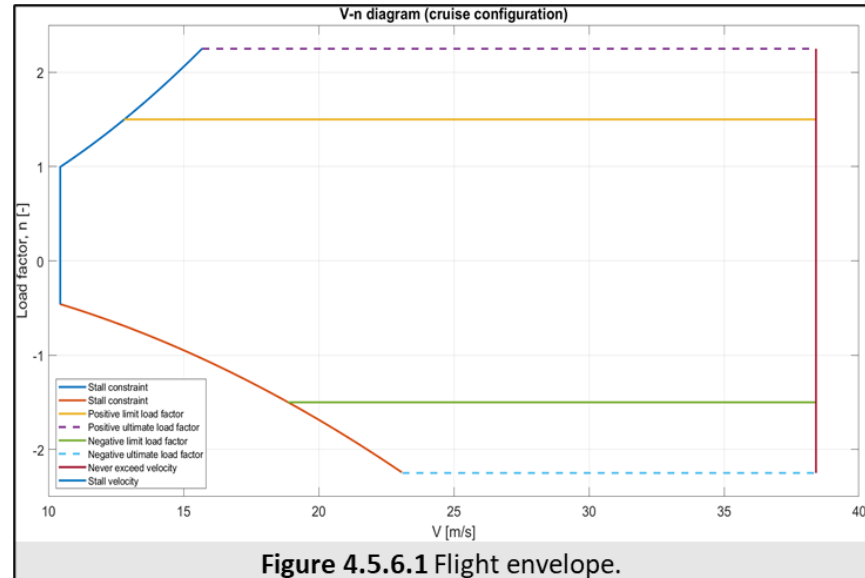


Figure 4.5.6.1 Flight envelope.

than the limit load factors respectively. These values describe a limit above which the aircraft will induce critical damage and could break apart. Thus, this limit must not be exceeded in any case scenario. The limit set by  $C_{L,max}$  is the boundary of the stall region above or below which the aircraft will stall. This curve can

be calculated directly from the definition of the load factor,  $n = \frac{L}{W} = \frac{\rho * V^2 * C_L * S}{2 * W}$ . Lastly, the boundary set by the velocity must not be exceeded, because increasing it further will increase the dynamic pressure higher than the design range of the aircraft. Since we cannot calculate it, literature<sup>[4]</sup> suggests a safety factor of 1.2 based on the maximum velocity the aircraft can achieve. This value was taken from Figure 4.5.3.1 and thus the never exceed velocity,  $V_{ne} = 38.4 \text{ m/s}$ . The flight envelope the cruise fight segment is presented in Figure 4.5.6.1.

#### 4.5.7 PROPULSION SYSTEM

For the propulsion system integration our options for the propeller selection are limited whereas the engine is mandatory to be an *AXI 2826/10 GOLD LINE V2* electric motor. The propeller options were split into two manufacturers, keeping the size of them the same, 10x6. We opted to select a propeller model from APC following our past experience with both manufacturers where we concluded that they are more rigid and perform better. Another plus for this selection is the available performance data which is provided by the official site of APC and helped us achieve more precise results. Since the models *LP10060E* and *LPB10060E* did not seem to have differences in performance we opted to pick the *LPB10060E* as it proposed less bureaucratic and logistical barriers. During the cruise flight segment, our propulsion system should meet the requirements for thrust while also keeping the propeller efficiency as high as possible. The required thrust during that segment can be calculated either from *Figure 4.3.6* or taken directly from *Figure 4.5.3.1*. The results are 2.76 N and 3.63 N. These values deviate as they are based on different methods of calculations. In order to have a complete analysis we opted to cover the needs of the higher value before the flight tests. Using the performance data mentioned above we kept two operational points for cruise speed of 20 m/s where  $\eta_p \approx 78\% @ 7000 - 8000 \text{ rpm}$ , the highest possible efficiency can be achieved. This means that the aircraft will fly, if not directly, very close to the optimal efficiency. Using an online tool which combines the electric motor, battery, RC control and propeller we managed to estimate the power supplied by the

propulsion system at cruise conditions which was  $P = 260 \text{ W}$  and thus this being the power available during cruise.

For the takeoff segment the propeller efficiency was calculated for a mean velocity of  $0.7 \cdot V_{LOF} = 7.7 \text{ m/s}$  and had a maximum value of 60.7% @5000 rpm, while also satisfying the mean required thrust of 2.91 N. For the climb segment it was calculated for the  $V_{R/C,max} = 24 \text{ m/s}$  and the maximum value was 80% @10000 rpm, while also satisfying the required thrust of 5 N.

The last parameter we needed to assess was the blade tip velocity which must not exceed a limit mostly set empirically based on the material the propeller is manufactured of. The propeller we used is made of fiberglass and so the limit set for composite propellers is 250 m/s<sup>[4]</sup>. The propeller follows a helical path through the air. A limit was set to 15000 rpm for thin electric propellers by the manufacturer. Moreover, the highest achievable aircraft velocity is 38.4 m/s. This set the tip's velocity at 203.15 m/s which was lower than the limit, meaning that in no case scenario shall our propeller break.

#### 4.5.8 PERFORMANCE SUMMARY

To summarize the whole performance assessment process Table 4.5.7.1 is presented including every parameter calculated as seen below.

Takeoff distance	$\eta_{p,takeoff}$	R/C <sub>max</sub>	$\eta_{p,climb}$	T <sub>req,cruise</sub>	P <sub>req,cruise</sub>	$\eta_{p,cruise}$	Range	Endurance	Landing distance
34.87 m	50%	3 m/s	60%	3.63 N	75.44 W	78%	2400 m	9 min.	52.58 m

Table 4.5.8.1 Summary of the aircraft's performance.

## 5 STRUCTURAL DESIGN

### 5.1 AIRCRAFT MASS & CG ESTIMATION

#### 5.1.1 FIRST WEIGHT ESTIMATION

An important first step into the design of AEOLUS was to estimate the mass fractions of the aircraft and at last its initial total weight ( $W_o$ ). The result of this analysis and its accuracy are critical while advancing into the next steps of the conceptual design phase. The method developed to estimate the aircraft's  $W_o$  is based on trade studies and correlations from literature<sup>[1], [5]</sup> while linear interpolation is applied between  $W_e/W_o$  and  $W_o$ . This method was expressed in code utilizing MATLAB software due to the large number of computational repetitions.

Taking into consideration the mission and flight plan described by the regulations of ACC 2022, we defined numerically the necessary factors that were either given, estimated, or demanded for the analysis. Those factors cover a large range of inputs regarding the efficiencies of the propulsion system (from battery to propeller), the aircraft category, the payload, the endurance as well as some flight parameters and how they value in each flight segment: takeoff, climb, cruise, loiter and landing.

The result of every analysis was evaluated such as to justify the needs of the mission and utilized from the Aerodynamics Design subsystem in order to define the constraints of the aircraft. This back-and-forth process between these two subsystems was completed through lots of iterations and the results are shown in Figure 5.1.1.1. As it can be observed, the curve presented below shows the variance of the  $W_o$  with respect to the energy density of the battery (ESB) for a specific cruise

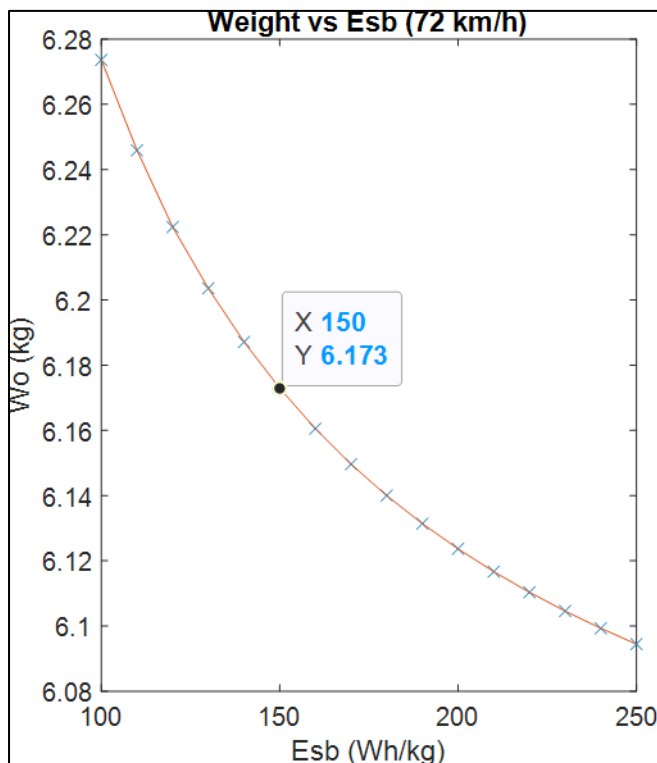


Figure 5.1.1.1  $W_o$  vs ESB for  $V_{cr}=20\text{m/s}$  &  $E=5\text{min}$

speed ( $V_{cr}$ ) at 20 m/s and 5min endurance ( $E$ ). The energy density of the battery was unknown at first but typical values for it can be around: 150 Wh/kg considering our application<sup>1</sup>. In that matter, our first  $W_o$  estimation was 6.17 kg, where 3.50 kg were for payload and approximately 2.39 kg were for  $W_e$  while the remaining weight was for the battery. This final result from the iterative process was validated from the constraints in *Section 4.1*.

$W_e/W_o$	$W_b/W_o$	$W_{pl}/W_o$
0.387	0.046	0.567

**Table 5.1.1.1:** Initial mass fractions

In addition, this result derived while considering the estimated  $W_e/W_o$  belongs in the category *home-built composite aircrafts*<sup>2</sup>. This is because we were planning to use composite materials from the beginning for reasons that are assessed in *Section 5.2.1*. The Table 5.1.1.1 shows the estimated mass fractions and other results from this initial analysis. It should be noted that these results were initial estimates, but they served as a starting point.

### 5.1.2 EMPTY WEIGHT ESTIMATION

As it can be seen from the diagram in *Attachments 1.1*, the  $W_e$  estimation was calculated right after the initial sizing of the aircraft which is performed by the Aerodynamics Design subsystem. Once again, Aerodynamics Design and Structural subsystems worked together in a feedback loop to obtain the best results possible regarding the aircraft's sizing, performance, stability, and  $W_e$  reduction. The Structural subsystem in this case provided the calculated mass and *CG* while, the Aerodynamics Design subsystem calculated the stability derivatives and estimated the aircraft's performance characteristics.

The  $W_e$  estimation in every different sizing iteration was calculated from a tool we have developed once again in MATLAB based on literature<sup>[1]</sup>. This tool has been developed to work with many different conventional aircraft configurations and utilizes only the sizing parameters of the aircraft's components and the limit load factor. The tool calculates via correlations the  $W_e$  of every component (main wing, fuselage, empennage) individually and sums them up for the  $W_e$ . You can find in Figure 5.1.2.2 the results from the final sizing iteration as well as the better approximations regarding the mass fractions in Figure 5.1.2.1. It should be noted that every sizing approach and different configuration we tried out in every iteration, is presented in *Section 4.3 Wing & Tail design* from the Aerodynamics Design subsystem.

$W_e/W_o$	$W_b/W_o$	$W_{pl}/W_o$
0.43756	0.047722	0.56244

**Figure 5.1.2.1:** Mass fractions

Furthermore, the  $W_e$  calculation does not consider the battery & ESC, the motor, and the additional component weight (GPS logger) so it must be added for the  $W_o$  calculation. Comparing the results with the previous analysis we observed that there was an error of 13% in the  $W_e/W_o$  while there was also an error of -4.9% in the  $W_o$  estimation. The margin of error in both cases is very small and under 15%, which is acceptable for the conceptual design phase, but also something that validates the previous method and simultaneously, verifies our mission parameters.

$W_{wing}$	$W_{H\_tail}$	$W_{Ve\_tail}$	$W_{fuselage}$	$W_{LG}$	$W_{battery}$	$W_{motor}$	$W_{add}$	$W_{payload}$	$W_o$	$W_e$
1.0829	0.15813	0.08859	0.39569	0.235	0.28	0.177	0.15	3.3	5.8673	2.5673

**Figure 5.1.2.2:** Empty weight estimation

It should be noted that in comparison with the previous analysis, the  $W_o$  decreased, while the  $W_e/W_o$  increased. This happened because of the available weight limitations which came up during the take-off assessment as seen in *Section 6*, while also the consideration of the limit load factor (*LLF*) set to be 1.5. In conclusion, to keep the estimated  $W_e$  constant we were mandated to "drop" our payload 5.7% to 3.3 kg.

<sup>1</sup> D. P. Raymer, "Chapter 20," in *Aircraft design: A conceptual approach*, Washington, D.C.: American Institute of Aeronautics and Astronautics, Inc., 1992, pp. 748-table 20.1.

<sup>2</sup> D. P. Raymer, "Chapter 3," in *Aircraft design: A conceptual approach*, Washington, D.C.: American Institute of Aeronautics and Astronautics, Inc., 1992, pp. 31-table 3.1.

### 5.1.3 CENTER OF GRAVITY

From the conceptual design phase diagram in *Attachments 1.1*, it can be observed that, the *CG* calculation occurred in parallel with the second weight estimation. The center of gravity and its percentage, regarding the wing's mean aerodynamic chord, are of vital importance during the aircraft's stability analyses. Considering the later, it opposed the following question to the Structural subsystem: *How is the CG going to be calculated without having to design every different aircraft configuration or sizing approach in CAD software?*

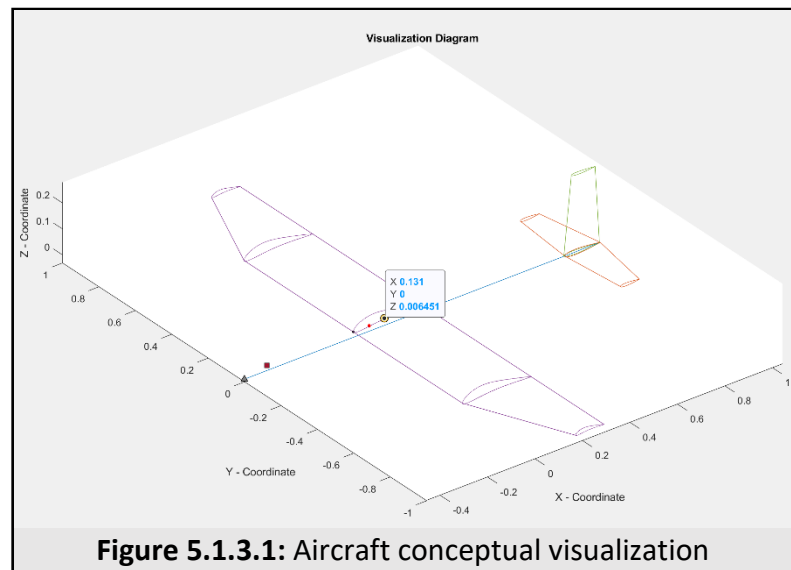


**Figure 5.1.3.1:** Aircraft conceptual visualization

To solve this time-consuming and recurring question we integrated code to the MATLAB tool which calculated the mass as described above. The tool utilizes all sizing parameters and airfoil shape as inputs to give an exact *CG* estimation, while the developed method is based on distinguishing our complex geometries in "finite elements". During this iterative process, we tried a lot of sizing approaches as described in *Section 4.3* in order to have the *CG* at the optimal position (36.5% *MAC*) but due to the restrictions from the rhombus shaped box it was very difficult to find the "golden ratio" between wing surface, stability, and battery placement. Battery placement was correlated in the tool with the *CG/MAC%*. Each time we calculated the optimal battery position to achieve the desirable *CG/MAC%* which was at last 36.5%.

Finally, the results of our analysis are presented in Figure 5.1.3.1. We shall note that the coordinates appearing, indicate the *CG* estimation in meters, while the grey rhombus marker represents the motor, and the red rectangle marker represents the battery. The cargo bay and payload have not been included in the *CG* calculation because we wanted the aircraft to be able to fly both with and without the cargo during the test flights. The idea is that the *CG* of the aircraft (without cargo) matches the *CG* of the cargo bay and payload along the x-axis in order to achieve stable flight in both cases.

We have also performed a *CG-Payload* sensitivity analysis, as it is depicted in Figure 5.1.3.2. The blue and orange curves represent specific payload positions (most forward and aft) while we vary the payload weight in those positions in order to see how it affects the *CG/MAC%*. The marked points show the limits of this analysis because there is a certain number of blood bags (weight) that can fit in those certain positions. It should be noted that in Figure 5.1.3.1 we can also see those extreme limits marked as two red dots, while their position in terms of *CG/MAC%* can be deducted from Figure 5.1.3.2 depending on the payload.

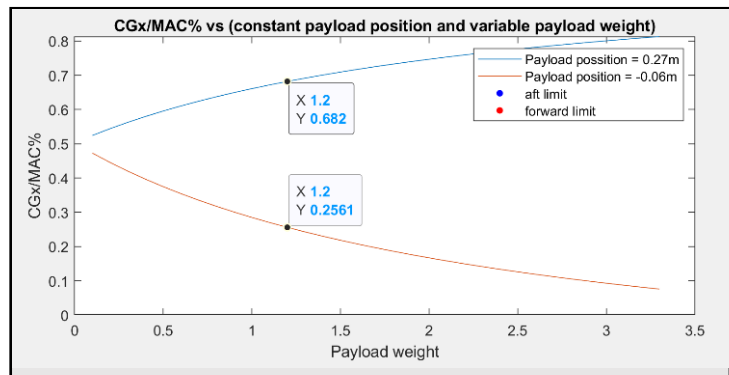


**Figure 5.1.3.2:** CG-payload position sensitivity analysis

## 5.2 MATERIAL SELECTION & MANUFACTURING PROCESSES

Up until this point, during the conceptual phase of the design, we haven't mentioned anything about selected materials or manufacturing processes. Our previous estimates were based solely on sizing, correlations, trade studies and low fidelity tools. The previous analyses helped to better define the design and gave us the necessary requirements to start the discussions regarding the process of material selection and manufacturing from the conceptual phase while it was finalized in the preliminary design phase.

### 5.2.1 MATERIAL SELECTION

Selecting materials for any type of application is usually performed in various steps, while the final selection arises through the process of elimination. As a subsystem we distinguished the process in 3 steps:

1. Gathering of mission and application requirements
2. Material research for a specific application
3. Process of elimination

The 1<sup>st</sup> step refers to the mission requirements that must be considered while selecting the most suitable material for our application. Requirements such as weight, performance, manufacturability, budget availability, ease of assembly, structural design principals, repairability and lifespan were taken into account. Some of these requirements were already assessed from the previous analyses and others were up for discussion and estimation. The 2<sup>nd</sup> step refers to the research we have done which is based on similar application studies and experience from our previous aircrafts. In a few words, during the 2<sup>nd</sup> step, we have “gathered” different materials suitable to be used in our application and

Composite	Conventional
Carbon Fiber	-
Fiber Glass	-
PVC foam	-
Aramid-Kevlar	-
Infusion Epoxy	5 min epoxy
Aluminum	-
XPS foam	XPS foam
Plywood	Plywood
Balsa wood	Balsa wood
-	Heat shrink film

**Table 5.2.1.1:** Optional material categories

Mission Parameter	Composites	Conventional
Lightweight	✓	✓
Structural Performance	✓	
Manufacturability		✓
Budget Availability	✓	✓
Easy of Assembly		✓
Structural Design	✓	
Repairability	✓	✓
Lifespan	✓	

**Table 5.2.1.2:** Elimination through specific mission parameters

distinguished them in 2 main categories. The categories and materials are presented on Table 5.2.1.1. The 3<sup>rd</sup> step refers to the process of finding the best materials for the aircraft by comparing them to one another using the mission requirements from step 1 and in some cases even conducting experiments.

We began the process of elimination by discarding the conventional materials category, even though at some major aspects (ease of assembly, manufacturability) those types of materials have the advantage. There were some important parameters in our mission we could

not sacrifice such as our structural performance and lifespan. Moreover, from our experience in composite structures, we have seen much better performance in terms of durability under stress while also the LLF gets larger for the same weight. We know that the methods of manufacturing and assembling composite materials are very complicated, but our previous aircrafts have given us the knowledge and experience to do so. Lastly, it should not be forgotten that the selected aircraft category from the first weight estimation was conducted considering “*Home-built composite*” aircrafts.

Moving on with the process of elimination, we found the need to discuss the type of our internal structures. We decided to go with the most conventional design i.e. having skins, spars, bulkheads, and stringers, with a semi-monocoque fuselage. Starting from the ribs, bulkheads, spars, formers, stringers and longerons, there were 4 potential materials - Balsa wood, plywood, aluminum, and composite “sandwich” panels (2 or 4 layers of carbon fiber woven fabric where in-between them is placed one 2mm thick PVC foam core material and infused with epoxy resin all together) - but there was also the option to replace them with XPS foam. The XPS foam option was eliminated quickly for the wing and fuselage because of manufacturing problems regarding the complexity of our geometries, although it was a great option for the tail as described in Section 5.3.3. Aerospace grade aluminum 6061-

Carbon Fiber Woven Fabrics						
	Tow	Warp	g/m <sup>2</sup>	Weave	E (GPa)	UTS (MPa)
1	3k	3k	220	Twill 2x2	235	4410
2	15k	15k	160	Twill 2x2	230	4900
3	15k	15k	160	Plain	230	4900

**Table 5.2.1.3:** Optional carbon fiber woven fabrics

T6 as well as plywood were discarded due to their weight and the remaining options were balsa wood and composite “sandwich” panels. Both options had approximately the same weight but from experiments and previous aircrafts we knew that the composite “sandwich” had a larger stress to weight ratio. In conclusion we used composite “sandwich” panels for every rib, bulkhead, spar, former, longeron or stringer on the aircraft. As for the skins, the clearest option was to go with *CFRP* (Carbon Fiber Reinforced Polymer) where in some areas of the fuselage’s skin it had to be *GFRP* (Glass Fiber Reinforced Polymer) to be RF transparent. Control surfaces as it is going to be explained in *Section 5.3.6*, will have an Aramid – Kevlar pivot point from the skins, as Kevlar, is a rip-stop, durable, and fatigue resistant material.

Moving on, it was a matter of selecting the most suitable carbon fiber, glass fiber and Aramid fiber fabrics, while also choosing the proper epoxy resin compatible with the fabrics, our application, and the manufacturing process. For the carbon fiber fabrics, we had three possible options as seen on Table 5.2.1.2. From the three we selected the first two because we opted to combine the increased stiffness of the first one while keeping the weight at a minimum with the second fabric as an outer layer in all skins. As for the resin, we decided to go with a fatigue resistant epoxy compatible with our fabrics and suitable for VIP (Vacuum Infusion Process) manufacturing process. Finally, the fiberglass fabric we selected was a 3k plain weave  $100 \text{ g/m}^2$  as it was not going to be used in the parts of the aircraft that experience excessive stress from the cargo. The Aramid fiber used, was a Kevlar 5 cm wide plain weave strip of  $170 \text{ g/m}^2$ .

Moreover, we have conducted experiments and in some cases FEM analyses with all the previously mentioned materials, to find the most suitable number of plies and ply orientation for every component of the aircraft.

### 5.2.2 MANUFACTURING PROCESSES

Composite materials seemed to be most suitable regarding our application, but there are a lot of downsides in terms of manufacturing mainly because they are demanding, time consuming, sometimes dangerous, and expensive. We tried to select the most suitable manufacturing process considering our requirements for weight, durability, and stiffness. These parameters can be controlled from the composite’s composition meaning the percentage of reinforcement in the matrix. Through literature [7], [8] we found that good composite compositions for *CFRP* and *GFRP* range from [70% Reinforcement and 30% Matrix] to [60% Reinforcement and 40% Matrix]. To obtain such results in our laminates we conducted experiments, every experiment was for a different manufacturing process as seen in Table 5.2.2.1

In every experiment the fabric was weighed before and after lamination, where the difference in weight was the weight of the

Manufacturing Process	Laminate composition
Hand Layup	[53% CF – 47% Epoxy resin]
Vacuum Infusion Process (VIP)	[67% CF – 33% Epoxy resin]
Wet layup with breather fabric under vacuum	[60% CF – 40% Epoxy resin]

**Table 5.2.2.1:** Manufacturing process and resulting laminate composition

matrix in the specimen. It should be mentioned that every one of these processes was performed at least once, for every different laminate composition (regarding both materials and number of plies). Having that in mind, we selected VIP for every skin and spar of AEOLUS, while the *wet layup with breather under vacuum* process was selected for the composite “sandwich” panels. Note that we also tried to infuse the resin into the composite “sandwich” panels but there was an excessive amount of waste resin flowing through the infusion mesh.

For the skins and the spars of the aircraft that were going to be infused, we applied the method of pattern making with a CNC router from a sponsor, and following that, we generated negative fiberglass tooling molds for the infusion process instead of carving negative molds directly with the CNC. This method, even though harsh and time consuming, increased the accuracy of our parts and allowed us to have control over any inaccuracies and defects caused in the pattern making process.

The rest of the components - ribs, bulkheads, stringers, formers and longerons - were cut from the composite "sandwich" panels by outsourcing them to a hydro-cutting machinery. For the assembly, it should be noted that we used small amounts of epoxy, infused with short glass fibers.

## 5.3 AIRCRAFT STRUCTURES

### 5.3.1 MAIN WING

To begin with, one of the most important features on a fixed wing UAV is its lift generation device, where in this case it is reassembled by the main wing. The main wing must withstand the loads in various stress conditions and generate the aerodynamic forces to lift the weight of the aircraft and its cargo. From a structural point of view, the main wing structure and its assembly with the fuselage play a huge role into ensuring a structurally flawless flight.

Considering our calculations during preliminary and conceptual design phases, the wing shouldn't weigh more than 1.08 kg and its structure must be as light as possible, while at the same time the wing must be in the position to withstand the loads during flight. With that in mind, before we began the discussions and analyses that had to do with the main wings structure, we needed to assess the mission requirements regarding the worst loading cases. Here came in to play the *LLF* (Limit Load Factor). The *LLF* was assessed from the conceptual design phase of AEOLUS and it is inextricably linked to the limit loading on our wing. Although, the wing must withstand under the Limit Loading and for that it must be multiplied with a safety factor in order to obtain the *ULF* (Ultimate Loading Factor). In our case, the value of the safety factor is selected to be 1.5 according to literature<sup>[9]</sup> for general aviation.

Considering all the above, the *UL* (Ultimate Load) was calculated as seen below. The *LLF* value for AEOLUS has been selected from the initial phases to be 1.5 and the  $W_o$  of the aircraft has also been accurately estimated at 5.867 kg.

$$UL = \text{Safety Factor} \cdot LLF \cdot W_o = 1.5 \cdot 1.5 \cdot 5.8668 = 13.2 \text{ kg} \quad \text{or} \quad F_{max} \cong 130 \text{ N}$$

In conclusion, the design point of failure for our wing is over the load of 130N, meaning that if the sum of all infinite point loads in the wing's loading distribution exceeds 130N the wing must fail, otherwise our design is heavier than needed. We estimated the lift distribution as is seen in Figure 5.3.1.1 to be that of a fully elliptical wing due to our similar geometry without taking into consideration lift loss and drag increase near the centreline because of the propeller, fuselage, and cargo bay. It should be noted that lift distribution is a fraction of the resultant force  $R$  while the other part is due to drag, this was considered later in the following analysis.

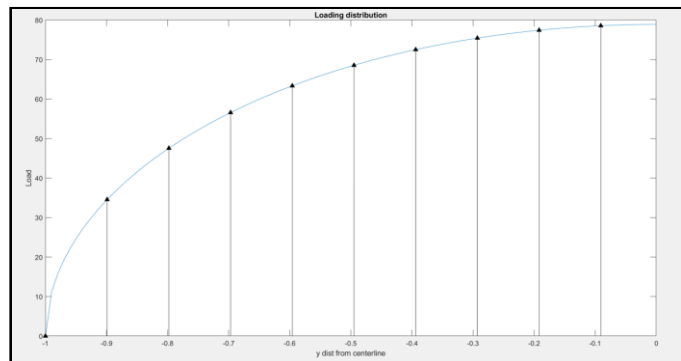


**Figure 5.3.1.1** Theoretical loading distribution on elliptical wing in steady level flight

The followed procedure after we had defined all requirements needed was a design and analysis loop, in which we designed the layout, and based on the results of every analysis changes were made to improve the main wing's structural performance.

We began the structural design approach by discussing about different types of spars and possible spar configurations. We landed on 2 different options: circular, and rectangular profile CFRP tubes. Circular CFRP tubes were discarded due to our experience with them and the difficulties we stumbled upon in manufacturing and assembly. Furthermore, rectangular profile CFRP tubes had the advantage of having 2 perpendiculars to the airfoil chord sides that increased wing stiffness and reduced wingtip displacements. Although the problem of assembling the wing structure was still standing with the rectangular spar, and not also that, they were heavier than the circular ones. Considering all the above came the idea of fabricating

our custom main and secondary spars in a single mold that had the exact geometry of the wing in order to make manufacturing much easier and the design much simpler.

**Custom Spars:** The spars of AEOLUS are shaped like plates placed perpendicular to the chord of the wing and are coloured in red in Figure 5.3.1.2. The spars are interconnected through the blue area to one another, which is also the area in contact with the upper skin that serves as, to reduce the risk of them being assembled incorrectly on the skin, or the risk of them being stressed in buckling under load. The green areas are the contact surfaces with the lower skin of the wing, and they are designed that way to ensure a good bond between the spars and the lower skin.

As for the placement inside the wing, the main spar is placed along the 25% of every span-wise chord length measuring from the leading edge, where the thickness of the span-wise airfoils tends to take the maximum value. The secondary spar is placed along the 50% where it's far enough from the main spar to reduce the risk of rotation along the y-axis, but not that far back to be very small in height.

Our spar design was influenced from literature<sup>[6]</sup> but in order to justify the shape of the spars we must consider the main type of strain on the wing which is bending along the z-axis. In general, we need a spar placed along the span of the wing that has such a cross sectional area to resist in any bending strain (we want as less flexion as possible). If we set a coordinate system on the wing as seen in Figure 5.3.1.8 and apply a load on the wing tip along the z axis the displacements  $w = w(z)$  can be approximated with the following differential equation. The product  $EI_{yy}$  is a measure of stiffness for isotropic materials, the equivalent laminate stiffness is given by:

$$\langle EI_z \rangle = \sum_i E_i I_{zi}$$

It should be noted that we used the following equation with caution because our spar laminated composite behaves as a quasi-isotropic material (polar plots are presented in Figure 5.3.1.4 for  $E_1$  and  $E_2$ ).

$$\frac{d^2w(x)}{dx^2} = \frac{M_y(x)}{EI_{yy}}, \quad I_{yy} = \frac{th^3}{12}, \quad \{M_y(x) \rightarrow \text{bending moment around } y\}$$

Young modulus  $E$  depends on material characteristics while the value of  $I_{yy}$  can be rearranged depending on design ( $t$  = thickness and  $h$  = height). To minimize the weight, we kept thickness to a minimum 3mm, and to maximize stiffness we kept  $h$  as high as possible (refer to main & secondary spar placement above). It should also be noted that  $h$  is raised to the 3<sup>rd</sup> power.

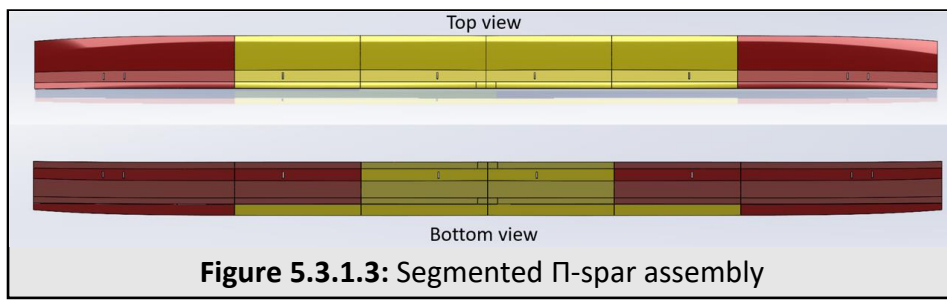


Figure 5.3.1.2 Main & Secondary spars configuration

From now on, to facilitate speech, we are going to refer to the spars as a single  $\Pi$ -like shaped spar. Considering the transportation box dimensions, the  $\Pi$ -spar was segmented in three sections: the mid-section (yellow section in Figure 5.3.1.3), and two side spars (red sections in Figure 5.3.1.3), with extensions that slide under the mid-section to ensure a good assembly surface.

As for the lamination we used two layers of 15k twill 2x2 carbon fiber fabric at ( $0^\circ|90^\circ$ ) and 2 layers of 3k twill 2x2 carbon fiber fabric at ( $-45^\circ|45^\circ$ ). Between the upper plies and the bottom plies of the Π-spar lamination, we placed 2mm PVC Foam Core, to increase thickness in order to avoid yield under buckling strain. Lamination sequence and material polar plots are presented in Figure 5.3.1.4. Note that  $0^\circ$  is defined as the direction along the span of the wing.

Moving on with our first design approach the second structural member of the wing that had to be discussed was the skins.

**Skins:** In order to select the number of plies and their orientation for the skins of the aircraft, we manufactured numerus laminate specimens utilizing VIP and comparing their final properties to one another. Specimens which consisted of one ply couldn't hold up under their own weight and so they were eliminated. Specimens that consisted of 2 plies of 3k twill 2x2 carbon fiber were very stiff but exceeded our weight limitations. As we have mentioned in the *Section 5.2.1*, specimens that consisted of 3k twill 2x2 at ( $-45^\circ|45^\circ$ ) and 15k twill 2x2 at ( $0^\circ|90^\circ$ ) carbon fiber fabrics were both lightweight and durable considering our application. It should be noted that for the lower skin sections, both plies are placed in the same orientation at ( $0^\circ|90^\circ$ ).

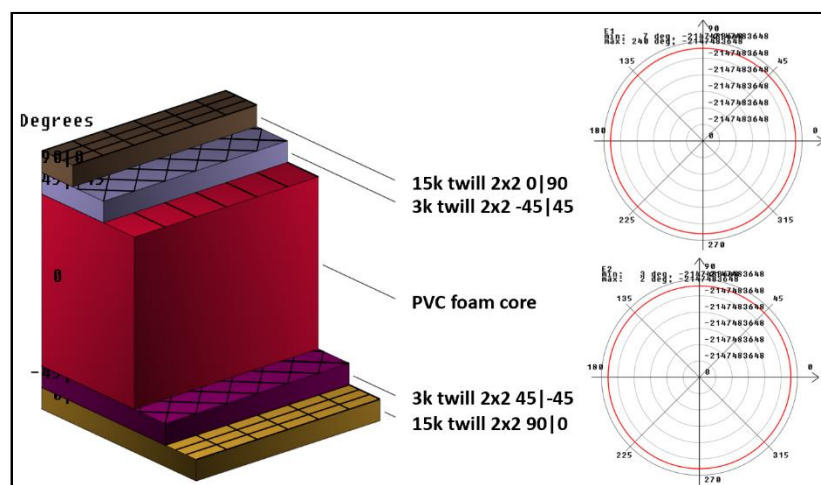


**Figure 5.3.1.4** Lamination sequence & Laminate polar plots for  $E_x$  and  $E_y$

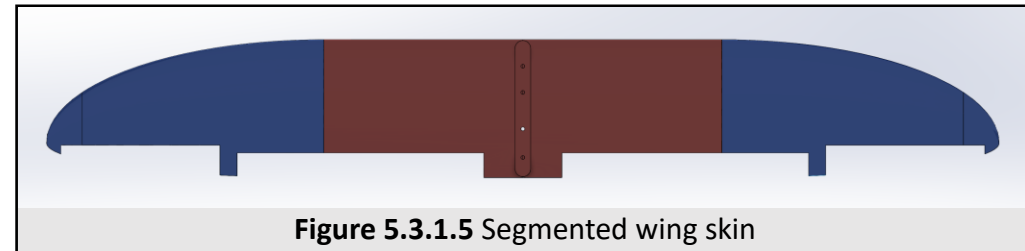


**Figure 5.3.1.5** Segmented wing skin

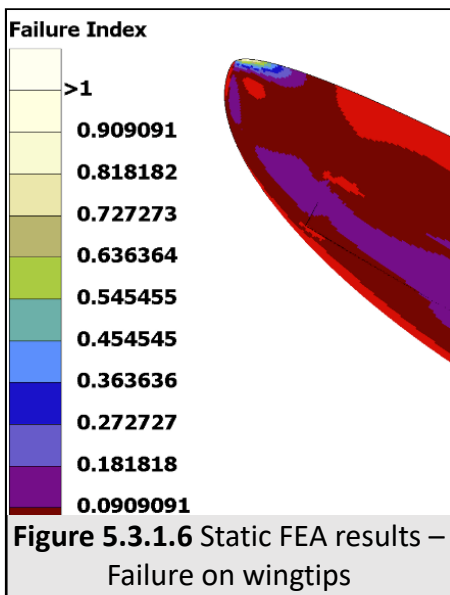


**Figure 5.3.1.6** Static FEA results – Failure on wingtips

Considering the requirements set by the transportation box, we had to split the wing skin into 3 segments: one rectangular shaped mid-section (red section from Figure 5.3.1.5) and two back tapered elliptical sections (blue sections from Figure 5.3.1.5). By splitting the skin in such a way, we managed to have a continuous mid-section in the area where stresses are most likely to concentrate.

Closing with our fist design approach, we performed static FEA on our wing and Π-spar assembly considering the loading distribution and its resultant maximum value from the requirements while also modeling the laminated properties for every part. We evaluated the results of the static analysis with the *Tsai-Wu Failure Criterion*<sup>[10]</sup>. As you can see from Figure 5.3.1.6, some elements near stress transition zones seemed to fail (colored in white and circled) near the wing tips of the wing and the elements near the center line of the spar also seemed to fail, see Figure 5.3.1.7.

Moreover, while evaluating the results of the analysis we found out that the upper surface of the spar lamination near the centerline was at risk of delamination, something that compromises the whole component and its fixation on the skin. Solving the delamination issue on the spar, we removed the bottom flanges which seemed to fail and extended the spar down to the fuselage. The overall solution to this problematic design was to add ribs in strategic places that would not only benefit the durability of our wing but also serve as end-planes for the control surfaces.

**Ribs:** As it is shown in Figure 5.3.1.8, we placed 12 ribs in total along the length of the wing, 8 ribs were placed at the end-planes of control surfaces, while 4 of them are positioned in the mid-length of every control surface. The ribs are spread throughout the wing evenly and help “transit” stresses between the upper and lower surface of the wing skin eliminating the chance of stress concentration at the wing tips (Figure 5.3.1.8) or the chance of the upper skin to suffer from buckling. We placed holes almost on every rib to limit stress “transition” and furthermore reduce weight, since every gram reduced is important. Every rib is designed with 2 slots that correspond to the main and secondary spars. Slots were also placed on the  $\Pi$ -spar for reasons that facilitate assembly and interlock the components.

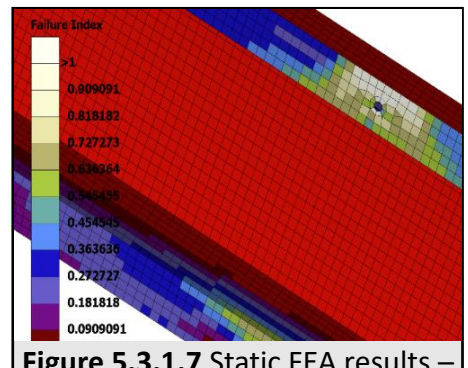


**Figure 5.3.1.7** Static FEA results – Failure on  $\Pi$ -spar flanges

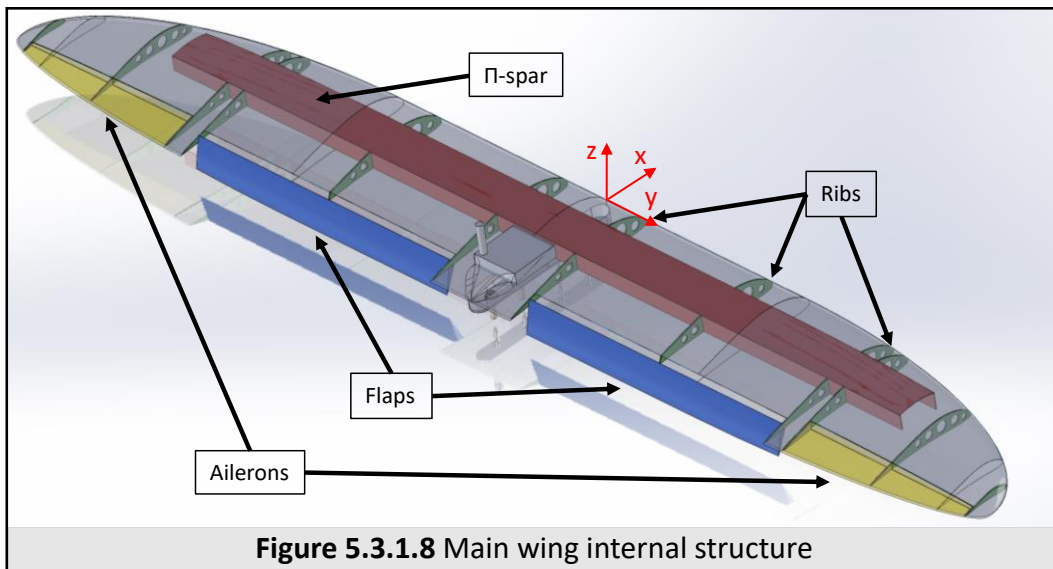


**Figure 5.3.1.8** Main wing internal structure

### 5.3.2 FUSELAGE

For the fuselage of AEOLUS, we tried to have things as simple as possible keeping in mind that it must serve the general purpose of keeping every part connected, aiming at the final arrangement of a complete and functional aircraft. The first phase of the fuselage design was regarding its outer shape. Our general goal was to reduce its aerodynamic “footprint”, so we generated the shape from a *NACA 0018* airfoil while also considering requirements given from the Aerodynamics Design subsystem such as the length of the fuselage (1500 mm) and its maximum depth (120 mm). The specific airfoil was selected because it was thin enough as to not increase the frontal area of the aircraft and not too thin so it wouldn’t fit the components that were going to be placed inside it. AEOLUS’s fuselage was designed to contain the battery, the *ESC*, the receiver, the motor and 2 servos (one for the elevator and one for the rudder). Also note that the shape of the fuselage at the nose was configured in such a way in order to fit around the motor and the fuselage tip got trimmed for the spinner.

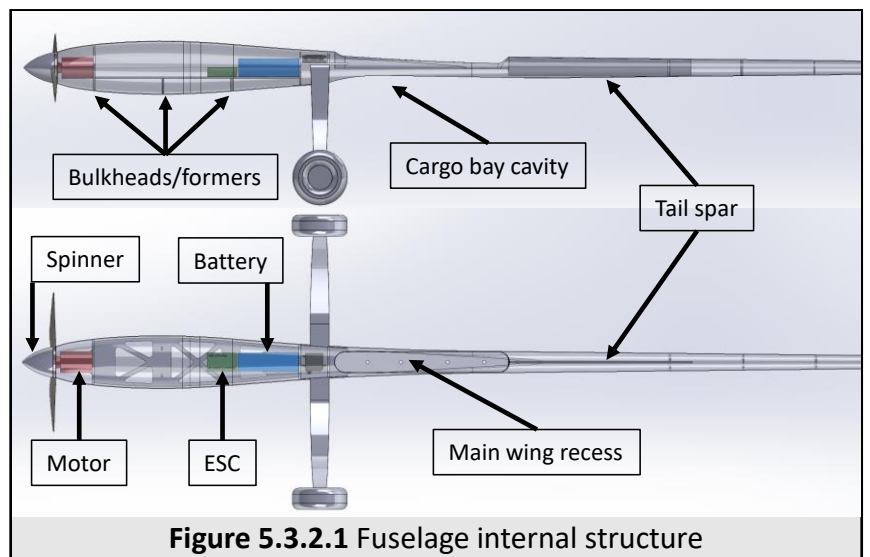


**Figure 5.3.2.1** Fuselage internal structure

The second phase of the fuselage’s design, revolved around the assembly of the aircraft and the modifications that had to be done for it to fit in the transportation box. Our first milestone was the design of the wing – fuselage – cargo bay assembly. The design of this particular assembly initiated from the

preliminary design phase, and it was finalised in the detailed design phase. Our goal was to lock the main wing's movement with the fuselage, while at the same time keeping the load from the cargo directly applied on the wing and not the fuselage. We made this possible with the use of a recess notch on the fuselage and an outdent oval shape on the lower side of the wing. As it is depicted in Figure 5.3.2.2, the wing's outdent sits perfectly inside the fuselage's notch and locks the movement of these components together around all 6 *DOF*. Regarding the second consideration, it can be observed in Figure 5.3.2.2 that the connection bolts are applied on the wing, while the opposing nuts, bolt on the cargo bay longeron. This ensures that the load from the cargo transfers directly on the main wing through four M8 bolts. Note that the areas coloured in red in Figure 5.3.2.2 have PVC foam core in-between 4 in total carbon fiber plies.

Considering the size of the transportation box, the fuselage was split in 2 parts: one forward and one aft. The section plane lies at the centre of the fuselage recess notch where the 2 forward bolts hold the front part of the fuselage and the aft 2 bolts hold the aft part of the fuselage. In simpler terms the fuselage is "squished" in-between the wing and the cargo bay. It should be noted that the fuselage was cavitated with the cargo bay at their contact surface as seen in Figure 5.3.2.1.

The second milestone revolved around the fuselage-tail assembly. In this case the assembly is depicted in Figure 5.3.2.3, the *CFRP* material from the fuselage tail arm wraps around the horizontal stabilizer's arm. Inside the arm of the horizontal stabilizer, we placed and glued a PLA 3D printed part which has a 3mm hole for an M3 bolt that secures the assembly. It should be noted that the bolt passes through the fuselage *CFRP* skin also, which is reinforced with formers and longerons in the most aft. The latter reduces rotational vibrations of the empennage around the fuselage's axis.

During the preliminary design, we decided that the best type for our fuselage design would be the semi-monocoque type, where the skin is strengthened not only by vertical structural members, but also by longitudinal members. This structure was designed to protect the fuselage from the loads it would receive, to provide support for both itself and other members, and to define the position of electronics. There are 10 vertical bulkheads/formers in total: one at the tip of the fuselage, where the motor rests (the motor bulkhead), two under the recess notch that dampen vibrations from the wing, two for the longitudinal bulkhead that supports the landing gear, three for the tail assembly and two for the horizontal bulkhead forward. Moving on we installed two longitudinal bulkheads to increase rotational stiffness along the axis of the motor shaft but also provide a space to install all electronics and main landing gear. The propeller and spinner assembly are depicted in Figure 5.3.2.4 below. It should be noted that the propeller is tightened on the motor spindle with one M6 hex nut while the use of a second one locks the first in place as seen in Figure 5.3.2.4.

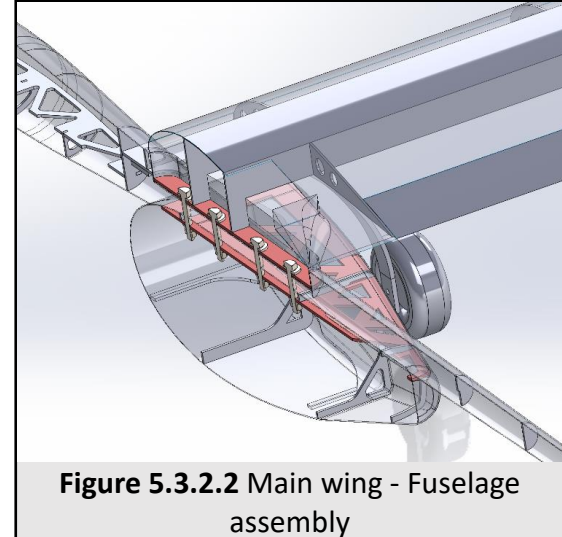


**Figure 5.3.2.2 Main wing - Fuselage assembly**

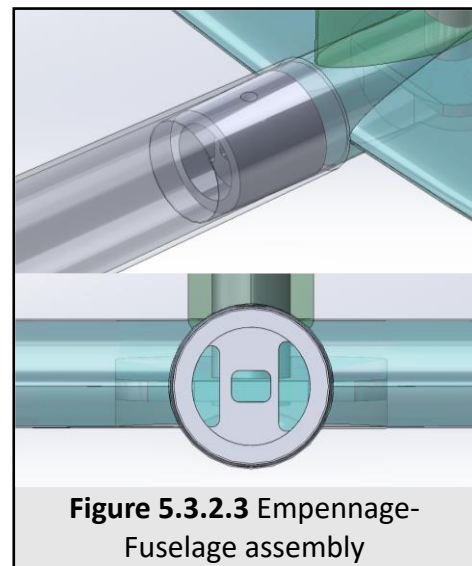
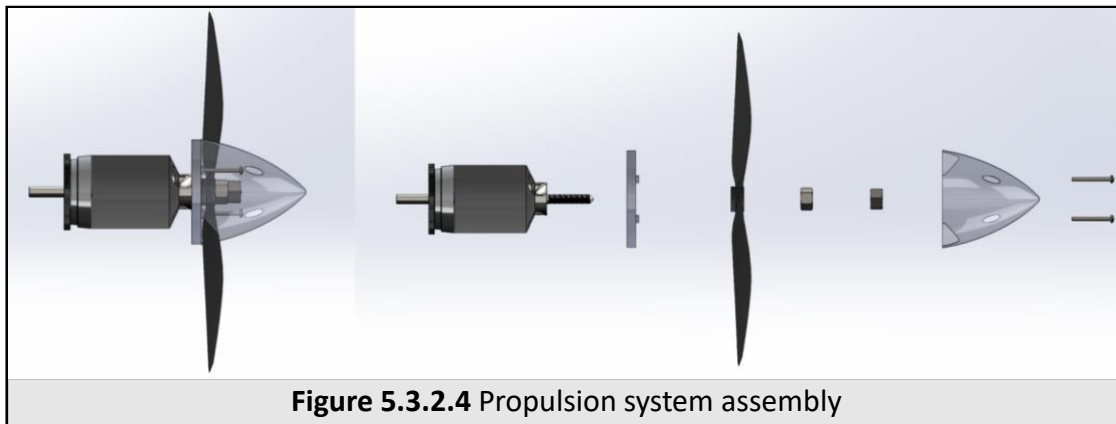


**Figure 5.3.2.3 Empennage-Fuselage assembly**

Regarding the laminates, fuselage skins have the same composition as the upper skins of the wing (*Section 5.3.1*) except from the lower forward skin which is going to be *GFRP* for RF transparency. All bulkheads/formers are manufactured from composite "sandwich" panels with 2 plies except the motor bulkhead that consists of 4 plies.



### 5.3.3 EMPENNAGE

As described in *Sections 4.3 and 4.4* the tail configuration which gave the best results in terms of stability was the conventional. During the preliminary design phase, the Structural sub-system was tasked to design the internal configurations of both the horizontal and vertical stabilizers as well as their assembly. The internal configuration design for both stabilizers, was driven taking into account their estimated weight from the conceptual phase of the design, as slight variations from that could result in a tail heavy and unstable aircraft.

The skins for both stabilizers are composed of 2 plies of CFRP similar to the upper wing skin but in this case in order to keep weight at a minimum we installed XPS foam (approximately 10 – 20 g were used) throughout their bodies instead of composite “sandwich” ribs. XPS foam was installed for three reasons: first, to limit the use of glass fiber infused epoxy, which in excessive amounts made the aircraft heavier, second, to hold the spars of both stabilizers as seen in Figure 5.3.3.1, and third, to avoid the skin from buckling. The horizontal stabilizer has a single composite CFRP spar where the plies are composed from 4 unidirectional strips of CF, whereas the vertical stabilizer has two tubular, 10x8 mm plain weave CFRP spars, that serve also as to “lock” the stabilizers together. As it can be seen from Figure 5.3.3.1 the vertical stabilizer spars are received into a composite “sandwich” plate sitting inside the horizontal stabilizer. The assembly is then secured with two M3 bolts running from the underside of the horizontal stabilizer, also holding the rear gear as seen in Figure 5.3.5.1.

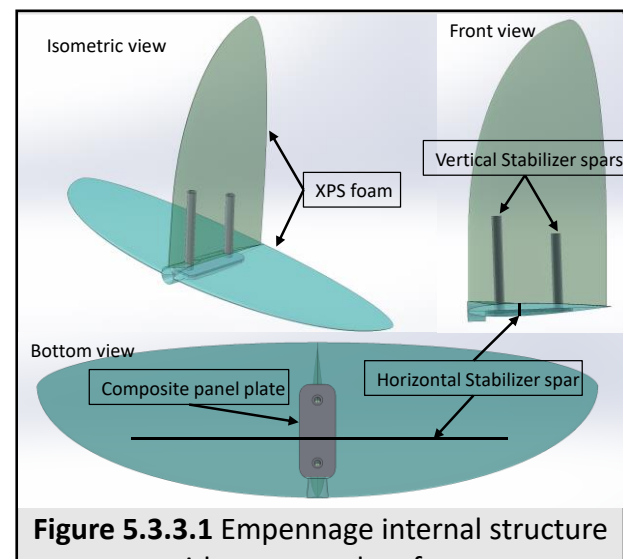


**Figure 5.3.3.1 Empennage internal structure without control surfaces**

### 5.3.4 CARGO BAY

Initially, our worries about the cargo bay were that the new payload would take more space than usual, since carrying blood bags requires a lot more volume rather than carrying something more solid and dense. After a small brainstorming session with the entire team, we ended up with 4 simple concepts designs. All 4 of them were then designed in CAD software, keeping their internal volume constant, just so we can get an idea about the dimensions that would be required for each design. When the initial design was finished, the Aerodynamics Design and the Structural subsystems chose the optimal cargo bay for our mission, one that was good in terms of aerodynamics, and at the same time could fit the payload without any issue.

After we had chosen our final design, a more detailed CAD was created, and this time the blood bags were modeled and inserted into the assembly as well, just so we can create the cargo without taking more space than necessary. By doing that, we were able to design a cargo bay that wouldn't be bigger than necessary, and at the same time keep the blood bags in a tight spot, all together, to avoid any extra movement that would occur during the flight, thus minimizing the sloshing effect on the payload. Another parameter for the cargo dimensions was to not be wider than the propeller diameter, in order for us not to lose any more lift

than necessary, as it would be inside the turbulent air, where lift loss already occurs from the propeller. The detailed assembly with the blood bags, also gave us a good approximation on where the *CG* would be, and that would give us the opportunity to position the cargo bay in a way that its *CG* lies with the *CG* of the aircraft unloaded, thus not affecting our stability for different cargo capacities.

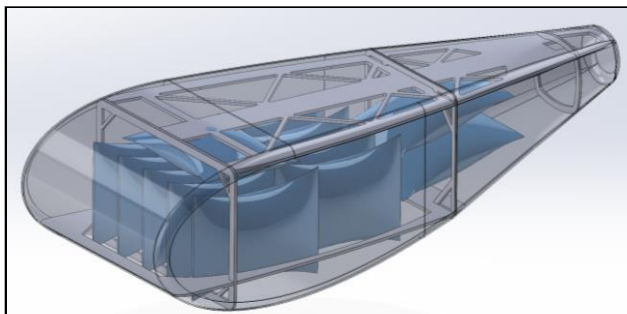


**Figure 5.3.4.1** Cargo Bay internal structure

The cargo bay is directly connected into the wing, so we can avoid making unnecessary assemblies. For example, if we were to connect it to the fuselage and then the fuselage into the wing, it would result in having more connections, and more things to be worried about failing. Because the assembly would be running across most of the cargo bay length, one big longeron was placed at the top, that would act as the center structure for the whole assembly. Three other bulkheads were placed in a position to hold the part as sturdy as possible, while also

create the tight space that was mentioned before. The structure described above can be seen in Figure 5.3.4.1. Every internal structural member used, is made from composite “sandwich” panels, while the skin is manufactured with VIP and consists of 2 plies: one 3k twill 2x2 carbon fiber fabric at  $(-45^\circ|45^\circ)$  and one 15k twill 2x2 carbon fiber fabric at  $(0^\circ|90^\circ)$ .

### 5.3.5 LANDING GEAR

The landing gear was one of the design topics that had us troubled from the conceptual phase of the design. Considering the regulations regarding the mandatory take-off and landing through a grass field, we started discussing about landing gear types and limitations that may arise from using a *taildragger* or a *tricycle* configuration. The answer to our troubles came from a session with the team’s Pilot, where he told us that he felt more confident to land a taildragger than a tricycle configuration. The pilot’s input on some characteristics of the aircraft is of significant importance and it should influence our design, that’s because if a worst-case scenario appears the aircraft won’t “hang by a small thread”.

We based our design around 4 principals<sup>3</sup>: 1) keeping the tail-down angle around  $10^\circ - 15^\circ$ , 2) keeping the angle between the *CG* of the aircraft and the vertical from the main wheel around  $16^\circ - 25^\circ$ , 3) the wing tips should not touch the ground on a  $5^\circ$  roll with the main gear on the ground, 4) have a reasonable amount of ground clearance for the propeller while the aircraft is horizontal to the ground.

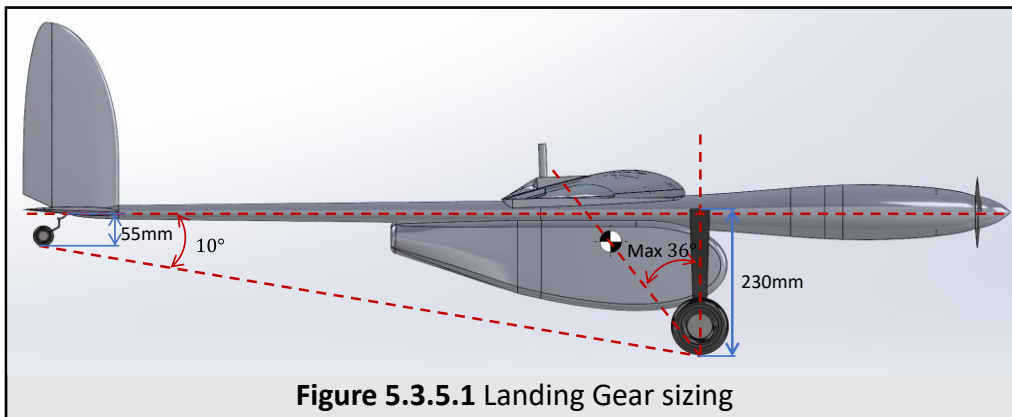


**Figure 5.3.5.1** Landing Gear sizing

Considering that the aircraft should rotate to the horizontal position before 40 meters during take-off we decided that a small tail-down angle around  $10^\circ$  was optional. To achieve this, we placed the main L.G. close to the main wing’s leading edge (considering principal

No.2), while its height  $230\text{ mm}$  (*L. G. + wheel radius*) was defined by the ground clearance for the cargo bay and the ground clearance for the propeller which was around  $100\text{ mm}$ . As for principal No.3 the width between both wheels of the main L.G is  $425\text{ mm}$  thus eliminating the chance of the wingtips touching the ground. Moreover, the tail gear was placed as far back as possible, while its height was selected to be  $55\text{ mm}$  (tail gear + wheel radius). The final dimensions are presented in Figure 5.3.5.1.

<sup>3</sup> D. P. Raymer, “Chapter 11,” in *Aircraft design: A conceptual approach*, 6th ed., Washington, D.C.: American Institute of Aeronautics and Astronautics, Inc., 2018, pp. 341–figure 11.4.

It should be noted that, although the angle between the vertical from the main wheel and the *CG* varies for different payload scenarios, it does not affect so much the rotation of the aircraft during take-off because the *CG* is only affected in the vertical direction. In Figure 5.3.5.1, we can observe the maximum value for this angle, which appears for maximum payload, and it does not obey principal No.2. Considering what is mentioned above there is another factor contributing to the rotation of the aircraft: our flaps, which generate a larger clockwise moment helping the aircraft overcome the weight of the payload during take-off.

All design and sizing parameters were defined from the conceptual phase while the actual components were selected based on these requirements in the preliminary phase. We chose the wheels for the main L.G to have an outer diameter of  $90\text{ mm}$  where the tail gear wheel was chosen to be  $32\text{ mm}$  in diameter. Both selections were based on the fact that our take-off and landing is going to take place in a grass field, and they are much rather on the larger side. Both the main and the rear l.g.s. are composite *CFRP* and their total weight is approximately  $180\text{ g}$ . It should be noted that in the case of the main L.G., we took the extra care for it to be wider than the cargo bay

### 5.3.6 CONTROL SURFACES

In the preliminary design phase, we discussed the topic of control surfaces assembly. There were 2 major ideas: Joining control surfaces with suitable interlocking PLA 3D-prints or utilizing Aramid – Kevlar woven strips from the VIP process step that later would be used as a skin pivot points. Considering the reliability, convenience, and weight of each option we concluded that the second one was the best for our application.

Note that the  $5\text{mm}$  Kevlar strip is placed on the inside of the lower skin of every part (in case of the vertical tail the right skin) and infused with resin via VIP simultaneously with the rest of the carbon fiber plies. The next step was to fully assemble every part and then cut out the control surfaces trying not to go through the Kevlar. With this method we created our non-removable, but at the same time movable, control surfaces. Finally, the control surfaces were connected to the servomotors by conventional aviation modelling equipment.

## 5.4 SUMMARY

In the beginning of *Section 5.3* we referenced that the design of internal configurations was strongly influenced from the estimated weight for each component which should not be exceeded, otherwise there was going to be a payload reduction. Below, in Table 5.4.1 we summarized the weights of the aircraft for every component as they have been once again estimated. This time the estimation considered every internal and external structural component as they have been presented in *Section 5.3*, while the difference with the previous weight estimations in *Sections 5.1.1, 5.1.2* is that in this case the method of approximating the weight is analytical and not correlated with the sizing or the performance of the aircraft. We derived these approximations taking into consideration the materials and their densities as well as the laminate composition of each part of the aircraft.

	Wing	Fuselage	Horizontal stabilizer	Vertical Stabilizer	LG (main & rear)	Other
Estimation from sizing	1.083 Kg	0.396 kg	0.158 kg	0.089 kg	0.235 kg	0.607 kg
Composites approximation	0.894 kg	0.384 kg	0.132 kg	0.057 kg	0.251 kg	0.647 kg
Composite bonding agent	$\approx 0.09\text{ kg}$	$\approx 0.07\text{ kg}$	$\approx 0.03\text{ kg}$	$\approx 0.02\text{ kg}$	-	-
Final approximation	0.984 kg	0.454 kg	0.162 kg	0.077 kg	0.251 kg	0.647 kg
Error	-9.1%	12.7%	2.5%	13.4%	-	6.5%

**Table 5.4.1** Comparison between sizing estimated weights and final weight approximations

It should be noted that we still call the following values for weight approximations, because the aircraft is composite and the laminate composition of every part regarding its percentages in reinforcement and matrix depend on the manufacturing process (*Section 5.2.2*). Furthermore, although the following approximations

contain the weight of the last bolt and nut on the aircraft, we could not include into the calculations the bonding agent that is going to be used in the assembly of the composite internal configurations. The bonding agent is referenced in *Section 5.2.2* and its final weight for every component was guessed in *Table 5.4.1* regarding our experience and the amount possibly needed for every internal composite configuration. Note that in the fuselage we also consider the cargo bay's weight.

	$W_e$	$W_o$
<b>Estimation from sizing</b>	2.56 kg	5.87 kg
<b>Final approximation</b>	2.54 kg	5.84 kg
<b>Error</b>	-0.7%	-0.5%

**Table 5.4.2 Final weight approximation**

As it can be observed the margin of error between each part can vary in size and it can affect slightly the CG of the aircraft, but as it was mentioned in *Section 5.1.3* we correlated the CG with the distance the battery is from the origin (main wing's L.E.) to avoid any chance of the aircraft being unbalanced. The correlation can be depicted in *Figure 5.4.1*. Moreover, as it can be observed in *Table 5.4.2*, the final empty weight and total weight are very close to the previous estimations occurring from sizing. It should be noted that the total weight was considered by adding to the empty weight our payload 3.3 kg.

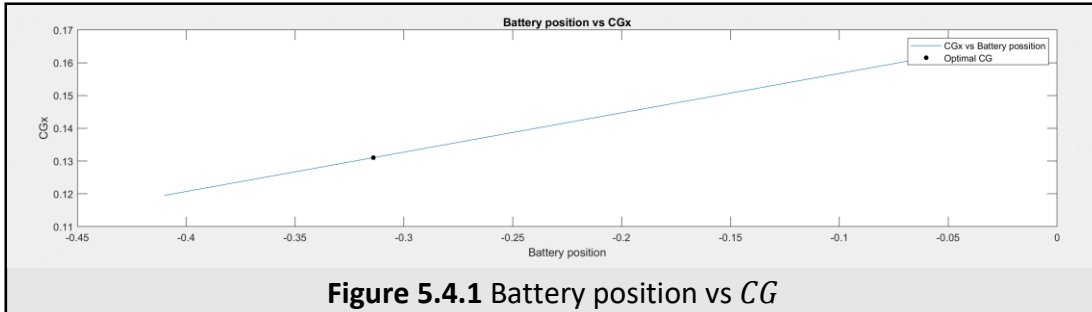


**Figure 5.4.1** Battery position vs *CG*

## 6 PAYLOAD PREDICTION

Our payload prediction was based both on the weight approximations referenced in *Section 5.1.2* and the constraints arising from the aerodynamic performance assessment of the aircraft in 2 different flight segments. Also note that we considered the produced lift as seen from *Figure 4.3.6* without flaps and from *Figure 4.5.1.1* with the use of flaps in order to be able to verify the lifted payload.

During the cruise segment, the aircraft will fly at a horizontal to the ground position with the wing's angle of attack being 2° equal to its incidence, and thus the predicted payload is based on the zero-angle of attack lift as seen in *Figure 6.1*. The corresponding formula utilized is:  

$$\text{Predicted payload (cruise)} = 7.2872 \cdot \rho - 2.56 \text{ [kg]}$$
 (also inserted in the diagram's legend). During cruise we can notice that the aircraft has the ability to lift 6.36 kg in total. By subtracting the empty weight approximation 2.57 kg we can predict the available payload at cruise which is 3.79 kg.

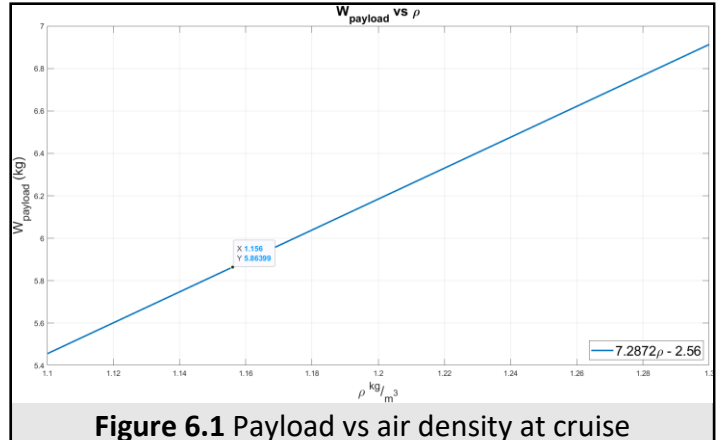


**Figure 6.1** Payload vs air density at cruise

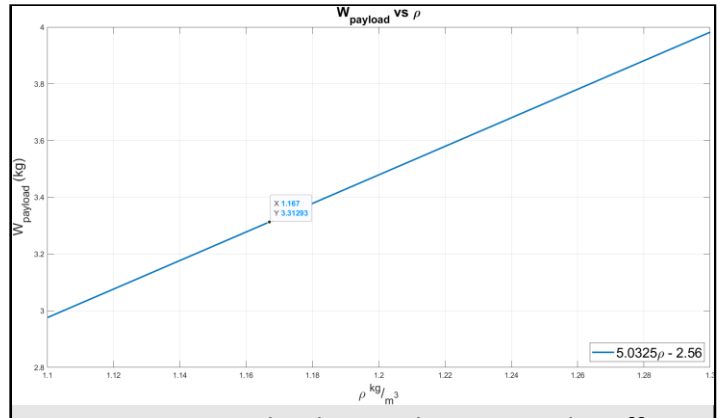


**Figure 6.2** Payload vs air density at take-off

Taking a step further, during takeoff, we focus on the liftoff segment where the aircraft will start to gain speed and rotate from the ground. During this segment, the pilot will slightly rotate the aircraft, but due to the landing configuration, the angle will be very small ( $\alpha = 1^\circ - 3^\circ$ ) while also the velocity will be less than the cruising velocity. This will pose a constraint on the lifted payload as seen in *Figure 6.2* and the

corresponding formula is  $\text{Predicted payload (takeoff)} = 4.8176 \cdot \rho - 2.56 [\text{kg}]$  (also inserted in the figure's legend) where we notice that the aircraft can lift 3.34 kg of payload. Finally, the payload is given with 100 g, 200 g and 300 g bags and thus the lifted payload will be limited to 3.3 kg with it being the final prediction. This final take-off constraint on payload weight, poses due to our wish to take-off before 40 m, where in that margin, the aircraft would not be able to gain the mandated velocity for take-off with the available payload set from the cruising segment.

## 7 AVIONICS

### 7.1 UAV ELECTRICAL EQUIPMENT

The UAV's electrical equipment includes the servomotors with their own battery pack, the motor, the Electronic Speed Controller (ESC), the main battery and the remote-control receiver. The Avionics subsystem was responsible for the selection of the components, their proper placement and wiring in the UAV. The ESC selected is the *HobbyWing Skywalker BL ESC 40A 2-3S LiPo 3A BEC*, which complies with the restrictions set by the competition for a minimum current of 30 A. For it to be connected to the battery, we soldered XT90 connectors to its wires. The main battery is the *Gens ace 5000 mAh 11.1V 3S 50C 3 Cell LiPo Battery*. After researching the available options for the battery type, we opted for a lithium-ion polymer battery (LiPo), as it is reliable and extensively used in the UAV field. The final model was selected in cooperation with the Aerodynamics subsystem, after considering parameters such as output voltage, capacity, discharge rate and battery weight. For the evaluation, the *eCalc-propCalc* online tool was also utilized, providing data about the propeller's performance given a battery, motor and propeller model. The *Corona DS238MG Digital Metal Gear 4.6kg servomotors* were selected after we calculated the maximum torque required for the deflection of each control surface using both a team-developed tool and the *Radio Control Info* online tool.

### 7.2 FLIGHT DATA COLLECTION

In order to receive flight data during the test flights, our team developed “*SensorBoard*”, a Printed Circuit Board (PCB) with various sensors, such as a GPS module, a barometer and accelerometer, connected to a microcontroller. The board also features a telemetry system developed with a LoRa module. This will enable us to receive live feedback for important flight parameters, such as speed and distance travelled by the aircraft, and thus to have measurable data for its performance. Though this board won't be used in the competition, it will help us in the test flights.

## 8 PROBLEMS ENCOUNTERED

After the postponement of ACC 2021, we had to face a lot of challenges such as the demotivation of old members, the departure of a lot of members from the team and the arrival of new ones that needed training. Furthermore, the COVID pandemic placed a lot of pressure on us, since for a long time it was impossible to get to our lab, and many orders were delayed.

We also had a lot of trouble with the mechanical processes, since we couldn't easily find machine shops that would take up our CNC machining orders. The late obtainment of our molds delayed our manufacturing timeline to a big extent. The bureaucracy of university funding made it difficult for us to place orders regarding the necessary materials and equipment, and in addition to that, the orders were taking too long to arrive. Our limited budget also placed a lot of strain on us.

## 9 OUTLOOK

Despite all the difficulties we have been facing, we are still going strong in our fight to have AEOLUS ready and airworthy. These past months haven't been easy for us, as there are continuous setbacks. However, the journey so far has been rewarding, filling us with new experiences and bringing us closer. We hope that by the end of the road, we will be able to achieve our goals, and that it will be worth our efforts. *We can't wait to host the next ACC in Thessaloniki Greece!*

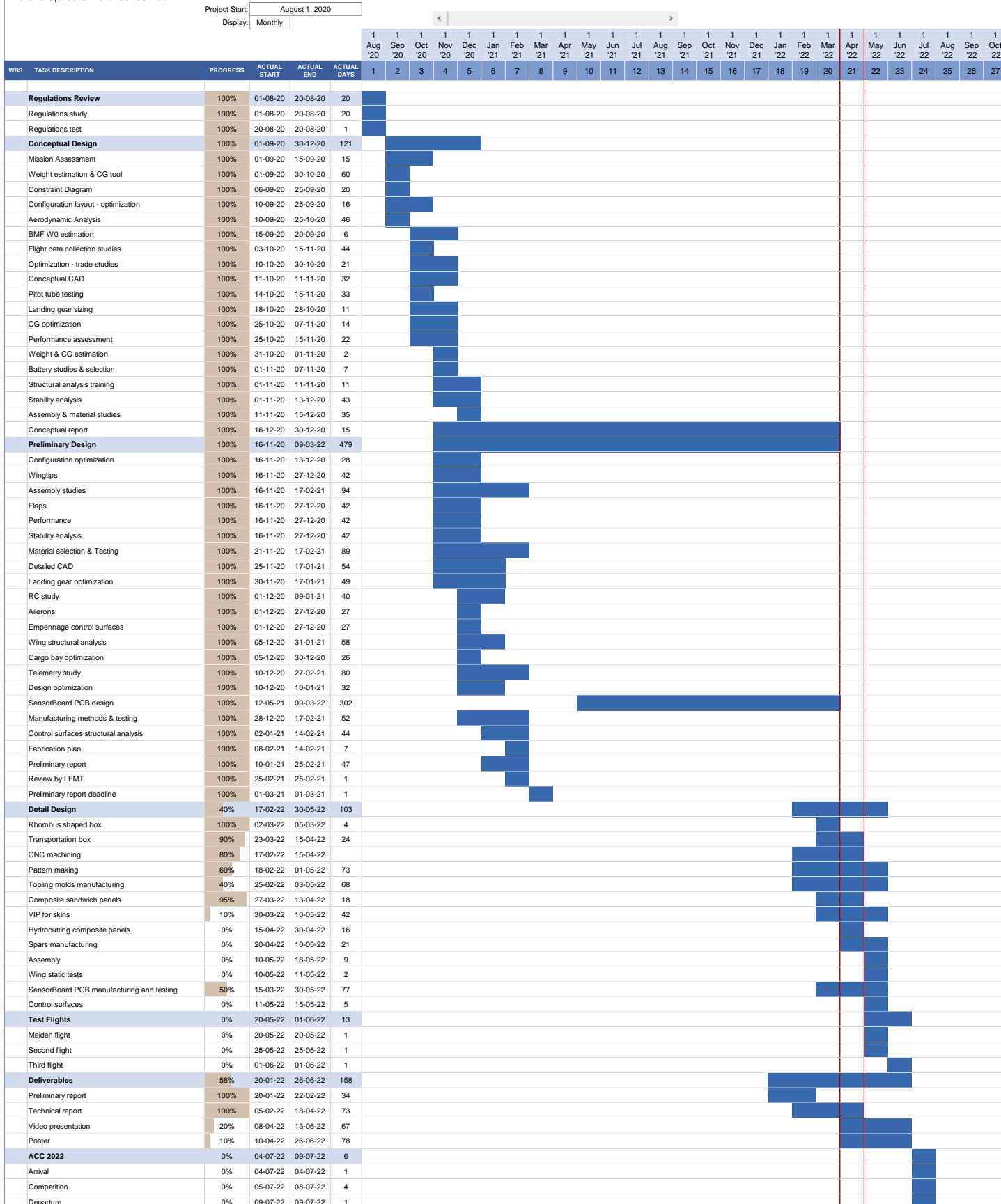
10 ATTACHMENTS

## 10.1 BUDGET & TIMELINE

AEOLUS BUDGET VARIANCE REPORT						
		Budget	Actual	Variance + / -		
<strong>OVERVIEW</strong>	Total expenses	€ 13,644.00	€ 10,174.75	€ (3,469.25)		
<strong>EXPENSE</strong>		Budget	Actual	Variance + / -		
<strong>Manufacturing</strong>						
Pattern making materials	€ 376.18	€ 211.18	€ (165.00)			
Tooling mold materials	€ 220.89	€ 426.29	€ 205.40			
CNC milling services	€ 5,500.00	€ 370.00	€ (5,130.00)			
CF fabrics	€ 376.73	€ 597.43	€ 220.70			
GF fabrics	€ 69.60	€ 69.60	€ -			
Aramid fabrics	€ 11.20	€ 11.20	€ -			
Hydrocutting services	€ 1,064.22	€ -	€ (1,064.22)			
Epoxy systems	€ 120.00	€ 238.90	€ 118.90			
<strong>Manufacturing Budget Variance</strong>	<strong>€ 7,738.82</strong>	<strong>€ 1,924.60</strong>	<strong>€ (5,814.22)</strong>			
<strong>Percent of Expenses</strong>	<strong>56.7%</strong>	<strong>18.9%</strong>	<strong>37.8%</strong>			
<strong>Equipment</strong>						
Protective Gear	€ 700.00	€ -	€ (700.00)			
Vacuum pump	€ 236.00	€ 252.00	€ 16.00			
Paint gun	€ 21.90	€ -	€ (21.90)			
Dremel	€ 59.90	€ -	€ (59.90)			
Solder & solder station	€ 80.00	€ 80.00	€ -			
<strong>Equipment Budget Variance</strong>	<strong>€ 1,097.80</strong>	<strong>€ 332.00</strong>	<strong>€ (765.80)</strong>			
<strong>Percent of Expenses</strong>	<strong>8.0%</strong>	<strong>3.3%</strong>	<strong>4.8%</strong>			
<strong>Logistics</strong>						
Competition fees	€ 1,750.00	€ 3,550.00	€ 1,800.00			
Travel	€ 1,500.00	€ 2,600.00	€ 1,100.00			
Equipment transportation	€ 350.00	€ -	€ (350.00)			
<strong>Logistics Budget Variance</strong>	<strong>€ 3,600.00</strong>	<strong>€ 6,150.00</strong>	<strong>€ 2,550.00</strong>			
<strong>Percent of Expenses</strong>	<strong>26.4%</strong>	<strong>60.4%</strong>	<strong>-34.1%</strong>			
<strong>Consumables</strong>						
Composite manufacturing consumables	€ 167.81	€ 338.58	€ 170.77			
Protective gear	€ 80.00	€ 80.00	€ -			
General manufacturing consumables	€ 100.00	€ 66.00	€ (34.00)			
Bolts	€ 15.00	€ -	€ (15.00)			
<strong>Consumables Budget Variance</strong>	<strong>€ 362.81</strong>	<strong>€ 484.58</strong>	<strong>€ 121.77</strong>			
<strong>Percent of Expenses</strong>	<strong>2.7%</strong>	<strong>4.8%</strong>	<strong>-2.1%</strong>			
<strong>Electronics</strong>						
LiPo batteries & bag	€ 82.00	€ 253.50	€ 171.50			
ESC	€ 19.00	€ 19.00	€ -			
RC controller	€ 89.65	€ 89.65	€ -			
Cables & connectors	€ 49.05	€ 49.05	€ -			
GPS logger	€ 129.00	€ 129.00	€ -			
<strong>Electronics Budget Variance</strong>	<strong>€ 368.70</strong>	<strong>€ 540.20</strong>	<strong>€ 171.50</strong>			
<strong>Percent of Expenses</strong>	<strong>2.7%</strong>	<strong>5.3%</strong>	<strong>-2.6%</strong>			
<strong>Miscellaneous</strong>						
Motors	€ 196.00	€ 240.00	€ 44.00			
Servo motors & cables	€ 64.61	€ 186.87	€ 122.26			
Landing Gear	€ 170.00	€ 218.00	€ 48.00			
Propellers & Accessories	€ 15.26	€ 59.22	€ 43.96			
Control surfaces assembly parts	€ 30.00	€ 39.28	€ 9.28			
<strong>Miscellaneous Budget Variance</strong>	<strong>€ 475.87</strong>	<strong>€ 743.37</strong>	<strong>€ 267.50</strong>			
<strong>Percent of Expenses</strong>	<strong>3.5%</strong>	<strong>7.3%</strong>	<strong>-3.8%</strong>			

AEOLUS

Aristotle Space & Aeronautics Team

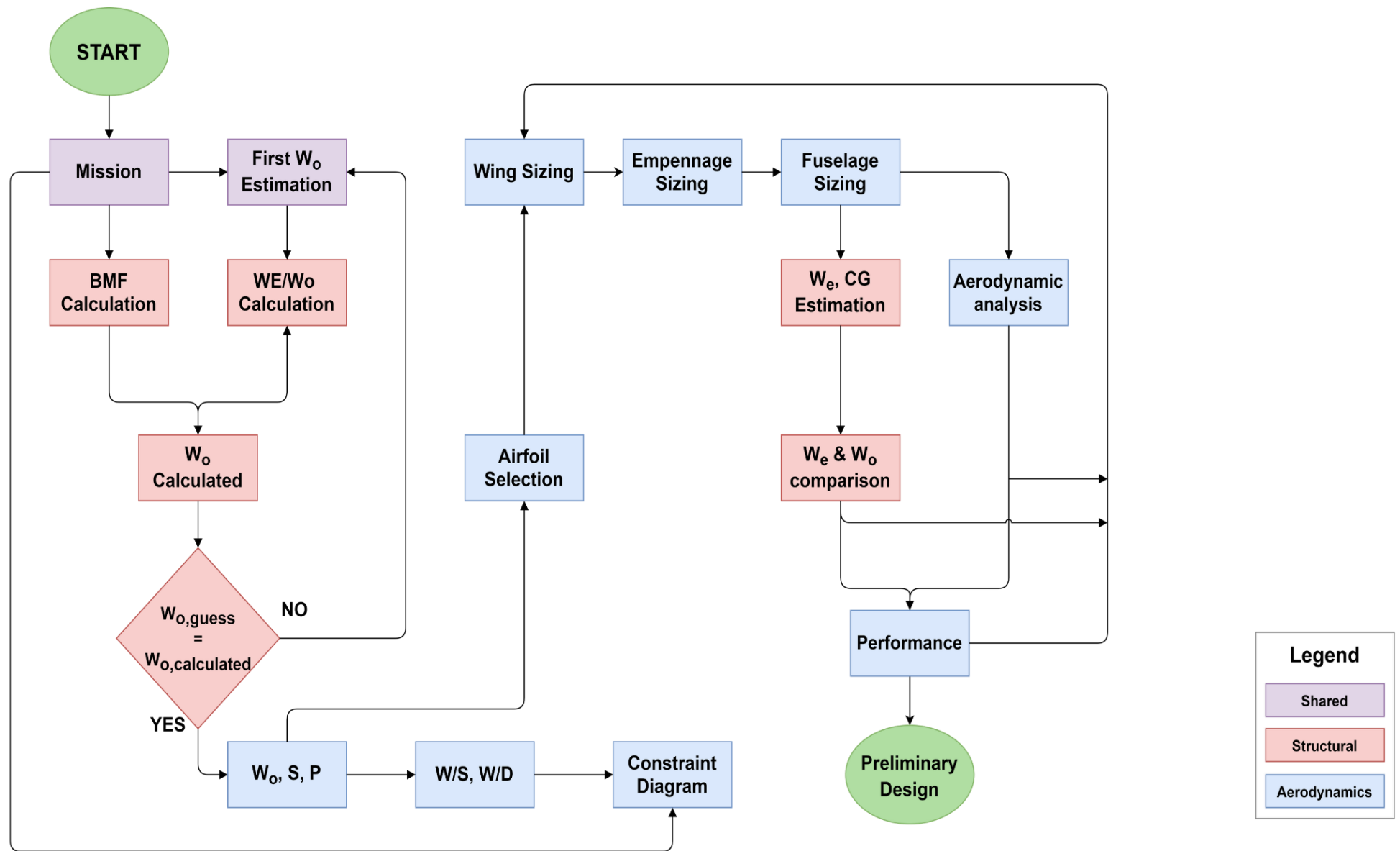


## 10.2 NOMENCLATURE

$AR$	Main wing's Aspect Ratio	-
$AR_h$	Horizontal tail's aspect ratio	-
$AR_v$	Vertical tail's aspect ratio	-
$\alpha$	Angle of attack	degrees
$\alpha_w$	Wing's angle of attack	degrees
$b$	Wingspan	$m$
$b_h$	Horizontal tail's span	$m$
$BMF, W_b/W_o$	Battery mass fraction (Battery mass over the aircraft's mass)	-
$CG$	Aircraft's center of gravity	$m$
$c_{root}$	Wing root chord	$m$
$c_{tip,min}$	Wing's tip chord minimum length	$m$
$c_l$	Airfoil lift coefficient	-
$c_d$	Airfoil drag coefficient	-
$C_{D,TO}$	Aircraft's drag coefficient during take-off	-
$C_{L,TO}$	Aircraft's lift coefficient during take-off	-
$C_L$	Aircraft's lift coefficient	-
$C_{L,max}$	Aircraft's maximum lift coefficient	-
$C_{L_{0,w}}$	Wing's lift coefficient at $0^\circ$ angle of attack	-
$C_{L_{\alpha,w}}$	Wing's lift coefficient slope	$\text{degrees}^{-1}$
$C_{L_{\alpha,h}}$	Horizontal tail's lift coefficient slope	$\text{degrees}^{-1}$
$C_D$	Aircraft's drag coefficient	-
$C_M$	Aircraft's pitching moment coefficient	-
$C_{M_{cg,w}}$	Wing's pitching moment coefficient around the center of gravity	-
$C_{M_{ac,w}}$	Wing's pitching moment coefficient around the aerodynamic center	-
$C_{M_{cg,f}}$	Fuselage's pitching moment coefficient around the center of gravity	-
$C_{M_{cg,h}}$	Horizontal tail's pitching moment coefficient around the center of gravity	-
$C_{m,\alpha}$	Aircraft's pitching moment coefficient with respect to the angle of attack	$\text{degrees}^{-1}$
$C_{m,q}$	Aircraft's pitching moment coefficient with respect to the pitch rate	$\text{degrees}^{-1}$
$C_{n,\beta}$	Aircraft's yawing moment coefficient with respect to the sideslip angle	$\text{degrees}^{-1}$
$C_{n,r}$	Aircraft's yawing moment coefficient with respect to the yawing rate	$\text{degrees}^{-1}$
$C_{n,p}$	Aircraft's yawing moment coefficient with respect to the rolling rate	$\text{degrees}^{-1}$
$C_{l,p}$	Aircraft's rolling moment coefficient with respect to the rolling rate	$\text{degrees}^{-1}$
$C_{l,r}$	Aircraft's rolling moment coefficient with respect to the yawing rate	$\text{degrees}^{-1}$
$C_{L,\delta e}$	Change in the lift coefficient with respect to the elevator angle	$\text{degrees}^{-1}$
$C_{m,\delta e}$	Change in the pitching moment coefficient with respect to the elevator angle	$\text{degrees}^{-1}$
$C_{n,\delta r}$	Change in the yawing moment coefficient with respect to the rudder angle	$\text{degrees}^{-1}$
$C_{l,\delta a}$	Change in the rolling moment coefficient with respect to the aileron angle	$\text{degrees}^{-1}$
$\Delta x$	Fuselage length increments	$m$
$\frac{\partial \varepsilon_u}{\partial \alpha}$	The change in local flow with angle of attack for each increment	-
$\frac{d\varepsilon}{d\alpha}$	Horizontal tail's change of downwash angle with angle of attack	-
$ESB$	Specific energy of battery	$Wh/Kg$
$E$	Endurance	$min$
$E$	Young modulus	$N/mm^2$

$\varepsilon_0$	Horizontal tail downwash at zero angle of attack	degrees
$i_w$	Wing's incidence angle	degrees
$i_h$	Horizontal tail's incidence	degrees
$i_f$	The incidence of the fuselage camber line to the fuselage reference line at the center of each fuselage increment	degrees
$I_{yy}$	Moment of inertia around y-axis	$Kg \cdot m^2$
$k$	Lift-induced drag constant	-
$k_2 - k_1$	The correction factor for the body fineness ratio	-
$L_f$	Fuselage length	$m$
$l_t$	Tail arm	$m$
$\lambda$	Taper ratio	-
$LLF$ or $n$	Limit Load Factor	-
$LL$	Limit Load	$N$
$MAC$ or $\bar{c}$	Mean Aerodynamic Chord	$m$
$M_y$	Bending moment around y-axis	$Nm$
$\eta$	Horizontal tail's efficiency	-
$\eta_{p,takeoff}$	Propeller efficiency during takeoff	-
$\eta_{p,climb}^V$	Propeller efficiency during climb	-
$\eta_{p,cruise}^V$	Propeller efficiency during cruise	-
$P_{req,cruise}$	Power required during cruise	$W$
$P/W$	Aircraft's power to weight ratio	$hp/lb$
$ROC$	Rate of climb	$m/s$
$ROC_{max}$ or $R/C_{max}$	Maximum rate of climb	$m/s$
$S$	Wing planform area	$m^2$
$S_a$	Aileron's planform area	$m^2$
$S_e$	Elevator's planform area	$m^2$
$S_r$	Rudder's planform area	$m^2$
$T_{req,cruise}$	Thrust required during cruise	$N$
$T/W$	Aircraft's thrust to weight ratio	-
$ULF$	Ultimate Load Factor	-
$UL$	Ultimate Load	$N$
$V_{cr}$	Cruise speed	$m/s$
$V_{stall}$	Aircraft's stalling velocity	$m/s$
$V_{ne}$	Aircraft's never exceed velocity	$m/s$
$V_{LOF}$	Aircraft's liftoff velocity	$m/s$
$V_{HT}$	Horizontal tail volume coefficient	-
$V_{VT}$	Vertical tail volume coefficient	-
$W_o$	Total mass	$Kg$
$W_e$	Empty mass	$Kg$
$W_e/W_o$	Empty weight fraction	-
$W_{pl}/W_o$	Payload mass fraction	-
$w_f$	Average fuselage width at each $\Delta x$	$m$
$W/S$	Wing loading	$lb/ft^2$
$w = w(z)$	Displacements vector in z direction	$m$
$\bar{x}_{cg}$	Aircraft's center of gravity position on the x axis	$\% \bar{c}$
$\bar{x}_{ac}$	Aircraft's aerodynamic center position on the x axis	$\% \bar{c}$

### 10.3 CONCEPTUAL DESIGN PHASE



#### 10.4 TECHNICAL DRAWINGS

8

7

6

5

4

3

2

1

F

F

E

E

D

D

C

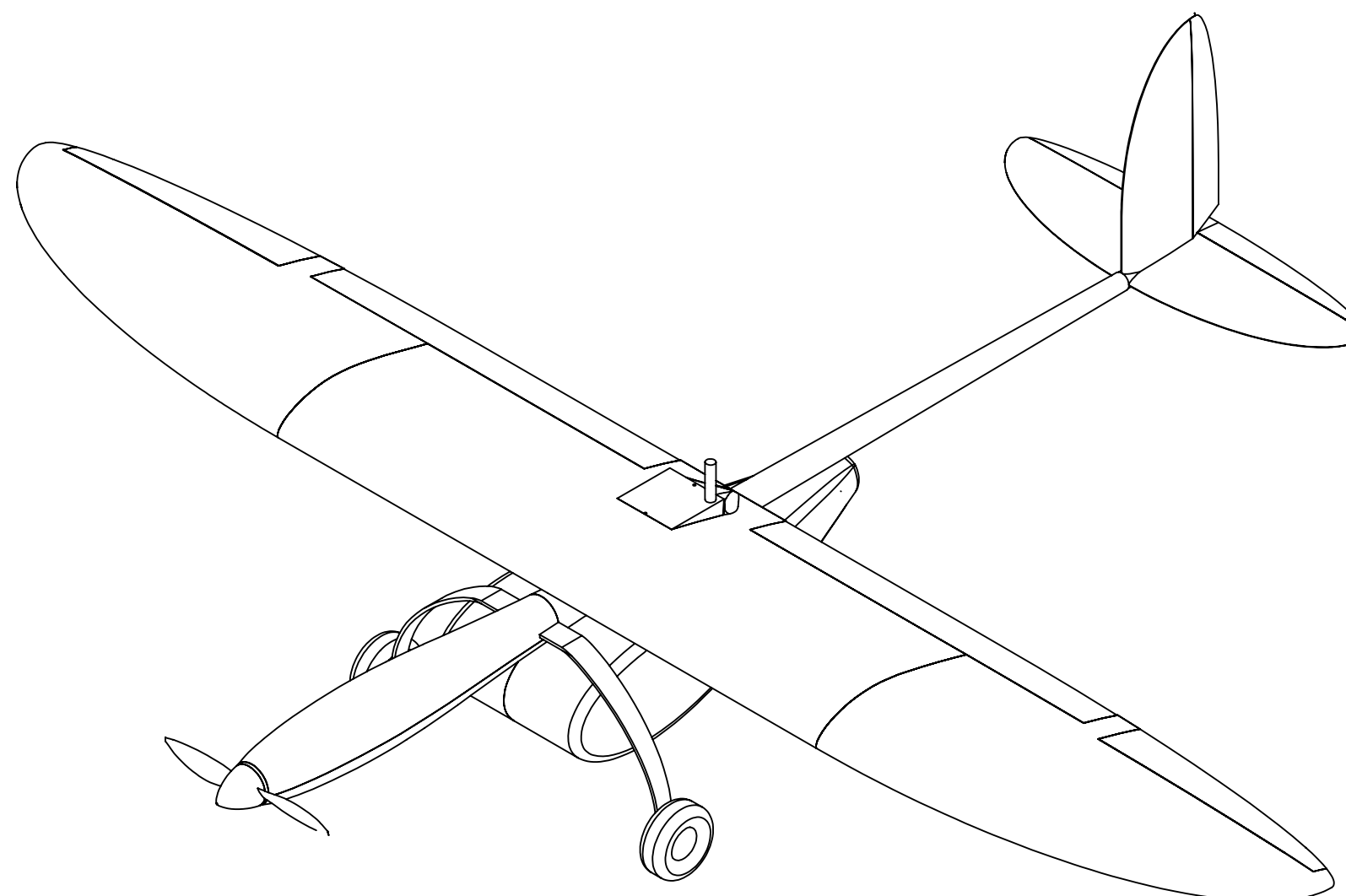
C

B

B

A

A



UNLESS OTHERWISE SPECIFIED:  
DIMENSIONS ARE IN MILLIMETERS  
SURFACE FINISH:  
TOLERANCES:  
LINEAR:  
ANGULAR:

FINISH:  
DEBURR AND  
BREAK SHARP  
EDGES

DRAWN  
CHK'D  
APP'D  
MFG  
Q.A.

NAME  
SIGNATURE  
DATE

MATERIAL:

WEIGHT:

DO NOT SCALE DRAWING

REVISION

TITLE:

A.S.A.T. - #10



DWG NO.

AEOLUS Isometric<sup>A3</sup>

SCALE:1:20

SHEET 1 OF 1

8

7

6

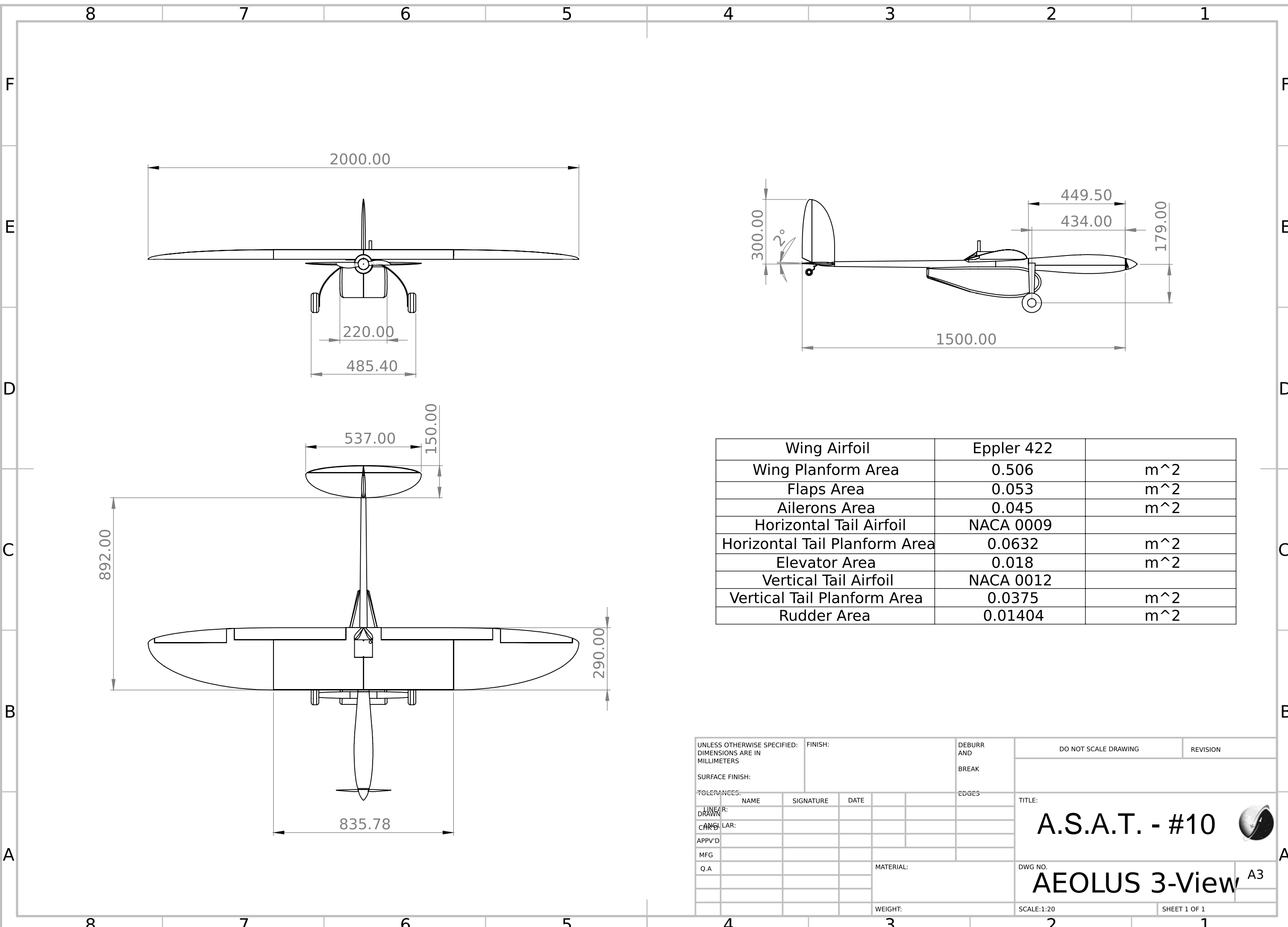
5

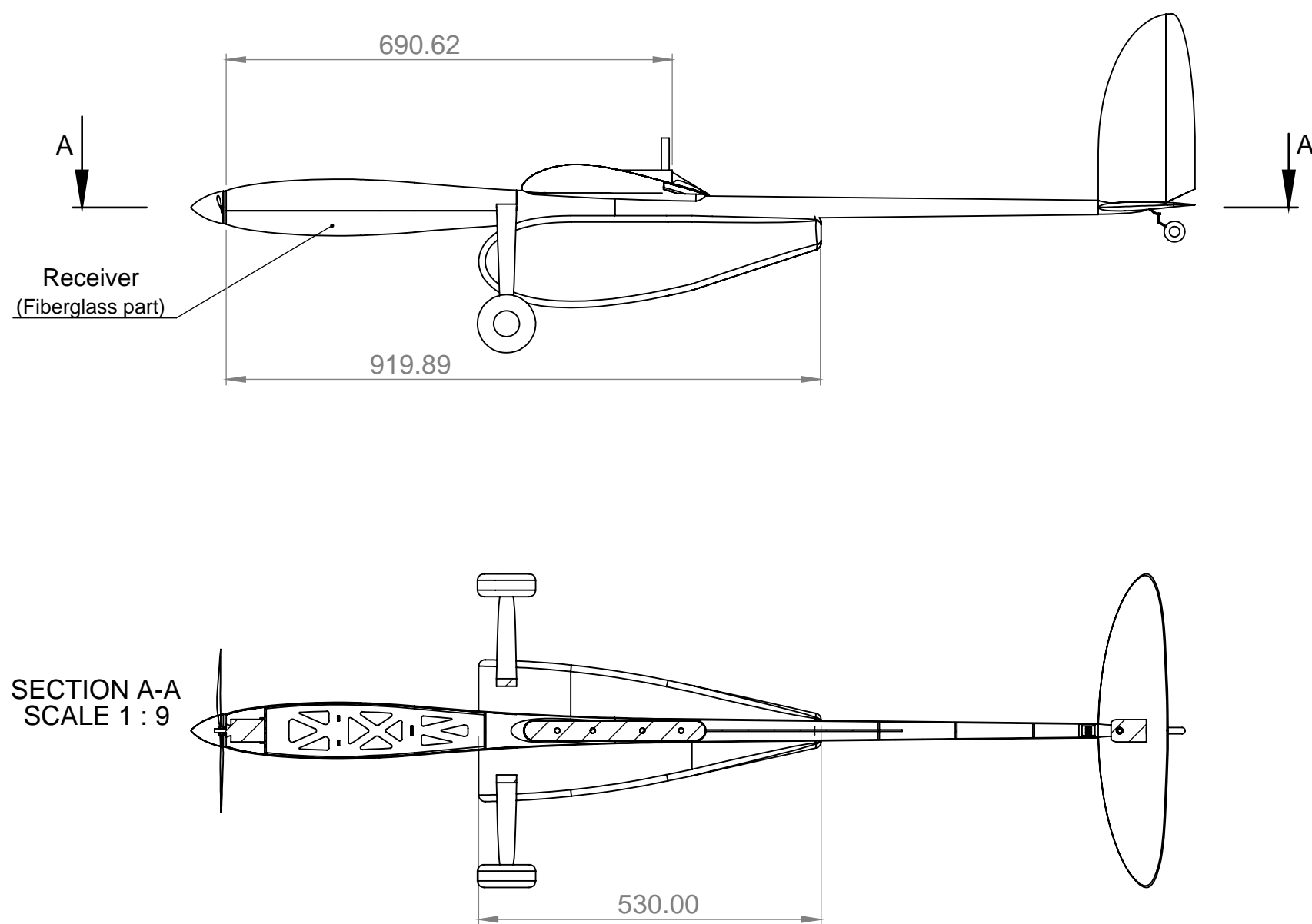
4

3

2

1





UNLESS OTHERWISE SPECIFIED: DIMENSIONS ARE IN MILLIMETERS SURFACE FINISH: TOLERANCES: LINEAR: ANGULAR:		FINISH:			DEBURR AND BREAK SHARP EDGES	DO NOT SCALE DRAWING	REVISION
	NAME	SIGNATURE	DATE			TITLE:	
DRAWN						A.S.A.T. - #10	
CHK'D							
APP'D							
MFG							
Q.A				MATERIAL:		DWG NO.	
						AEOLUS Section	
			WEIGHT:		SCALE:1:20	A3	
						SHEET 1 OF 1	

8                    7                    6                    5                    4                    3                    2                    1

F

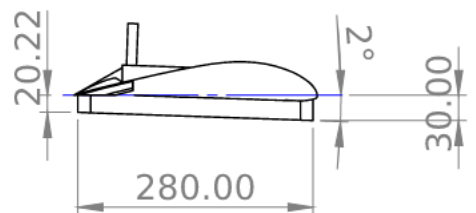
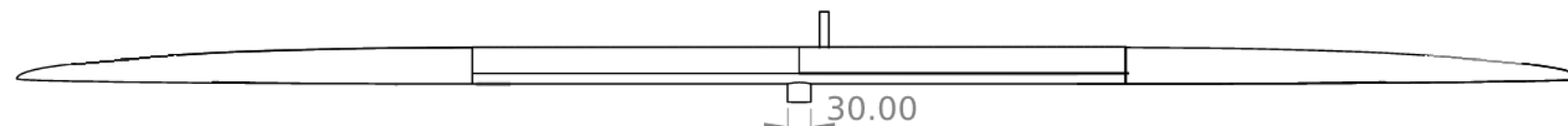
F

E

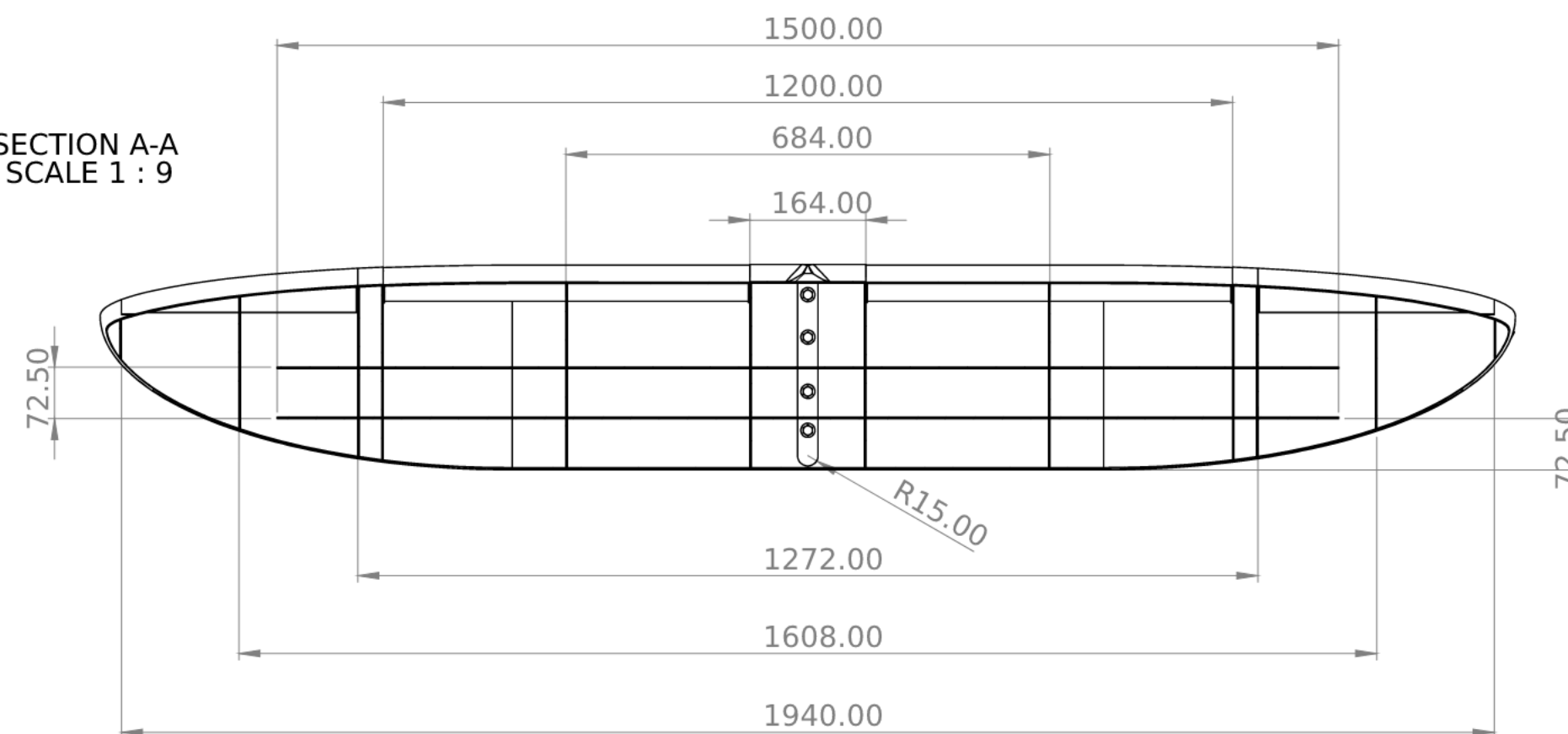
E

A

1



**SECTION A-A  
SCALE 1 : 9**



UNLESS OTHERWISE SPECIFIED: DIMENSIONS ARE IN MILLIMETERS		FINISH:			DEBURR AND BREAK	DO NOT SCALE DRAWING	REVISION
SURFACE FINISH:							
TOLERANCES:		NAME	SIGNATURE	DATE		EDGES	TITLE:
LINEAR: DRAWN:							A.S.A.T. - #10
ANGULAR:							
APP'D							A
MFG							
Q.A				MATERIAL:	DWG NO.		A3
			WEIGHT:		SCALE:1:20	SHEET 1 OF 1	

## 11 BIBLIOGRAPHY

1. D. P. Raymer, *Aircraft design: A conceptual approach*, 6th ed. Washington, D.C., 6th: American Institute of Aeronautics and Astronautics, Inc. , 2018.
2. S. Gudmundsson, *General Aviation Aircraft Design: Applied Methods and procedures*, 1st ed. Oxford, UK: Butterworth-Heinemann, 2014.
3. J. Roskam, “Part VI: Preliminary Calculation of Aerodynamic, Thrust and power characteristics,” in *Airplane Design*, Lawrence, Kan., Kansas: DARcorporation, 1987.
4. M. H. Sadraey, *Aircraft Design - A systems engineering approach*. Sussex, UK: Wiley, 2013.
5. S. Thyagarajan and N. Sharma, “Aircraft Mass Estimation Methods,” *International Journal of Engineering and Management Research (IJEMR)*, vol. 4, no. 5, pp. 170–178, 2014.
6. D. Gay, S. V. Hoa, and S. W. Tsai, *Composite materials: Design and applications*. S.l.: CRC PRESS, 2003.
7. F. C. Campbell, *Manufacturing Processes for Advanced Composites*. Oxford: Elsevier, 2004.
8. P. Morgan, *Carbon fibers and their composites*. Boca Raton: Taylor & Francis, 2005.
9. D. Howe, *Aircraft loading and structural layout*. John Wiley And Sons Ltd, 2004.
10. M. W. Hyer and S. R. White, *Stress analysis of fiber-reinforced composite materials*, Original edition. Lancaster, PA: DEStech Publications, Inc, 2009.
11. R. C. Nelson, *Flight stability and automatic control*, 2nd ed. Chennai: McGraw-Hill Education (India) Private Limited, 2010.